CHARACTERIZATION OF GEOTHERMAL RESOURCE IN THE OLKARIA SOUTH EAST FIELD USING MULTIDIMENSIONAL MAGNETOTELLURIC DATA INVERSION

EUNICE WAMBUI WACHIRA

MASTER OF SCIENCE

(Geothermal Science)

JOMO KENYATTA UNIVERSITY

OF

AGRICULTURE AND TECHNOLOGY

2024

Characterization of Geothermal Resource in the Olkaria South East Field using Multidimensional Magnetotelluric Data Inversion

Eunice Wambui Wachira

A Thesis Submitted in Partial Fulfillment of the Requirements for the Degree of Masters of Science in Geothermal Science of the Jomo Kenyatta University of Agriculture and Technology

2024

DECLARATION

This thesis is my original work and has not been presented for a degree in any other University.

Signature: ……. Date: ……

Eunice Wambui Wachira

This thesis has been submitted for examination with our approval as the University Supervisors.

Signature: ……. Date: ……

Dr. Maurice O. k'Orowe, PhD

JKUAT, Kenya.

Signature: ……. Date: ……

Dr. Justus Maithya, PhD

JKUAT, Kenya.

Signature: ……. Date: ……

Dr. Anna Mwangi, PhD

KENGEN, Kenya.

DEDICATION

I dedicate my thesis to my loving family for their endless love, support and encouragement throughout my pursuit for education. I hope this achievement will fulfill the dream they envisioned for me.

ACKNOWLEDGEMENT

I am thankful to the Almighty God for the gift of life and good health which made it possible to complete my work.

I am greatly indebted to African Development Bank together with the Ministry of Education for giving me financial support to pursue my Masters, words alone cannot explain how grateful I am indeed to them. I would like to thank KENGEN for allowing me to use their data.

This work would not have been complete without the generous support from my supervisors, Dr. k'Orowe, Dr. Maithya and Dr. Anna who spent many hours reading the manuscript I so often presented and their diligence in offering guidance and advice throughout the work. I also acknowledge and thank them for their patience with me.

I also extend my gratitude to my family and friends for their love and words of encouragement that kept me motivated. They were always beside me in every step that I took. I acknowledge my friend Claire Kimeli for the support and the motivational discussions throughout my work. I wish to acknowledge the exceptional support and patience from my loving family, my husband John and my children Joseph and Elsie they offered for the entire period of my studies.

May God bless you all.

TABLE OF CONTENTS

LIST OF FIGURES

LIST OF APPENDICES

ABBREVIATIONS

1-D	One Dimension
2-D	Two Dimensions
3-D	Three Dimensions
EM	Electromagnetic
MT	Magentotelluric
TE	Transient Electric
TEM	Transient Electromagnetic
TM	Transient Magnetic

LIST OF SYMBOLS

$\boldsymbol{\rho_a}$	Apparent Resistivity
σ	Conductivity
μ	Magnetic permeability
ε	Electrical permittivity
η	Electric charge density
Ω	Ohm
$\boldsymbol{\pi}$	Pi
B	Magnetic induction
E	Electric field
H	Magnetic intensity
D	Electrical displacement
j	current density
k	Wave number
Z	Impedance

ABSTRACT

One of the seven blocks that make up the Greater Olkaria Complex is Olkaria South East field. There are few wells that have been drilled, therefore the area is continuously being explored. Olkaria south east field is characterized by numerous surface manifestations such as fumaroles and altered ground, faults and structures that trend in the NE-SW direction. Most of the drilled wells are not in production and they experience temperature reversal at depth. Therefore, it is important to understand the physical properties of the Olkaria south east geothermal system. This information would be key in delineating the presence of caprock, reservoir, heat source and other geological structures controlling the system. To achieve this 23 MT data stations were used. The purpose of these geophysical data was to facilitate imaging of the subsurface geothermal structure with a view of characterizing and delineating the extent of the geothermal resource. MT data analysis was done to derive a dataset suitable for defining the resistivity model of the Earth from the observed MT data. The spatial median filter approach was used to correct the static shift effects of the MT datasets. Swift-skew, bahr-skew, ellipticity, and phase tensor dimensionality investigations revealed reduced skews at short periods and higher skews at long periods, revealing 1D and 2D characteristics at shallow depth and significant 3D structures at depth. 1D and 2D inversion were performed to generate resistivity models of Olkaria south East field. 3D MT inversion of Olkaria South East datasets using the ModEM program was performed to obtain the resistivity structure of the field. Generally, the inverted resistivity model fits the MT data very well, as demonstrated by the data misfit curves. Resistivity profiles were obtained from the 3D model to cut across the known geological structures in order to characterize the resistivity structure in the field. Since the profiles pass through the same soundings as in 2D inversion, a joint interpretation was made based on the two models. From the 2D and 3D resistivity models three layers have been revealed. The first layer has a high resistivity (~80 Ωm) which could be interpreted as the unaltered volcanic rock formation possibly from the pyroclastic cover. The second layer has a low resistivity (5- 10 Ωm) interpreted as the cap rock. The low resistivities are attributed to alteration minerals such as smectites and illites. The third layer has a relatively high resistivity (> 80 Ωm) and is interpreted as the geothermal reservoir. The resultant 3D resistivity models are generally similar to the two-dimensional (2D) inversion models; however, the deeper portion of the 3D model seems to be more realistic than that of the 2D model. From the conceptual model, Olkaria geothermal field reservoir is characterized by high resistivities and a drop in temperatures at the intercept of the intrusion. It can therefore be concluded to be as a result of cold inflow from the two faults transversing the field, majorly the Olobutot fault.

CHAPTER ONE

INTRODUCTION

1.1 Overview

Geothermal energy is the natural heat that is stored within the earth. The resource is manifested on the earth's surface in the form of hot springs, fumaroles, altered ground and steaming grounds. It is clean, abundant, and reliable renewable energy source, which is not affected by short-term fluctuations in the weather (Ballzus et al., 2000).

Kenya is potentially endowed with a huge geothermal resource due to the presence of the Kenya rift system. The records for the Olkaria power plants in Kenya (Lagat *et al.*, 2007; Kanda *et al.*, 2011; Omenda & Simiyu, 2015) show that once installed, maintenance costs are low and availability is high. The current total geothermal installed capacity in Kenya amounts to nearly 835.5 MWe contributing to almost 30% of total power generation in the country (KPLC, 2018).

Geothermal energy exploration in Kenya began in the 1950s with surface exploration that led to the drilling of geothermal wells at Olkaria, Menengai geothermal fields and Eburru. Currently, more than 200 wells have been drilled in the Greater Olkaria geothermal field while six wells drilled in Eburru, and at least fifty at Menengai (GDC, 2018; Omenda & Simiyu, 2015).

High enthalpy prospects are mainly located within the Kenya Rift Valley, where they associate closely with Quaternary volcanoes. Olkaria geothermal field is the leading producer so far with a current installed capacity of 833.2 MWe from the five power plants owned by Kenya Electricity Generating Company (KenGen) and Orpower4. The Oserian flower farm also has 4 MWe installed for its use and About 10 MWt being utilized to heat greenhouses and fumigate soils (Omenda & Simiyu, 2015).

The Olkaria reservoir is mainly characterized by dynamic liquid-dominated system. However, due to long term production, well discharge in some sections of the field is steam dominated, with about 15% water and 85% steam (Ouma, 2010).

Geophysics techniques have been used in the investigation of geothermal prospects since they give detailed information of the subsurface without drilling (Telford *et al*., 1990; Parasnis, 1997). Geophysical methods, such as the magentotelluric (MT) approach, which is increasingly commonly used to explore natural resources, including geothermal, can detect zones of low resistivity that are connected to geothermal reservoirs. This decrease in bulk resistivity in a rock mass is frequently caused by the higher temperatures and salinities of the pore water and concurrently greater rock alteration associated with geothermal locations (Naidu,2012).

1.2 Characteristics of a Geothermal System

A geothermal system can be described schematically as convecting water in the upper crust of the earth in a confined space which transfers heat from a heat source to a heat sink usually the free surface (Hochstein, 1990). A geothermal system as shown in Figure 1.1 is made up of three major elements namely, heat source, reservoir and caprock. A reservoir is a volume of hot permeable rocks from which the circulating fluids extract heat. Overlaying the reservoir is a cover of impermeable rocks and connected to a surficial recharge area through which meteoric water can replace the fluids that are extracted by boreholes or escape through springs. The heat source can either be a high temperature > 600^{o}C magmatic intrusion that has reached relatively shallow depths approximately 5 to 10 km, or as in certain low temperature systems, the earth's normal temperatures that increases with depth (Dickson & Fanelli, 2005).

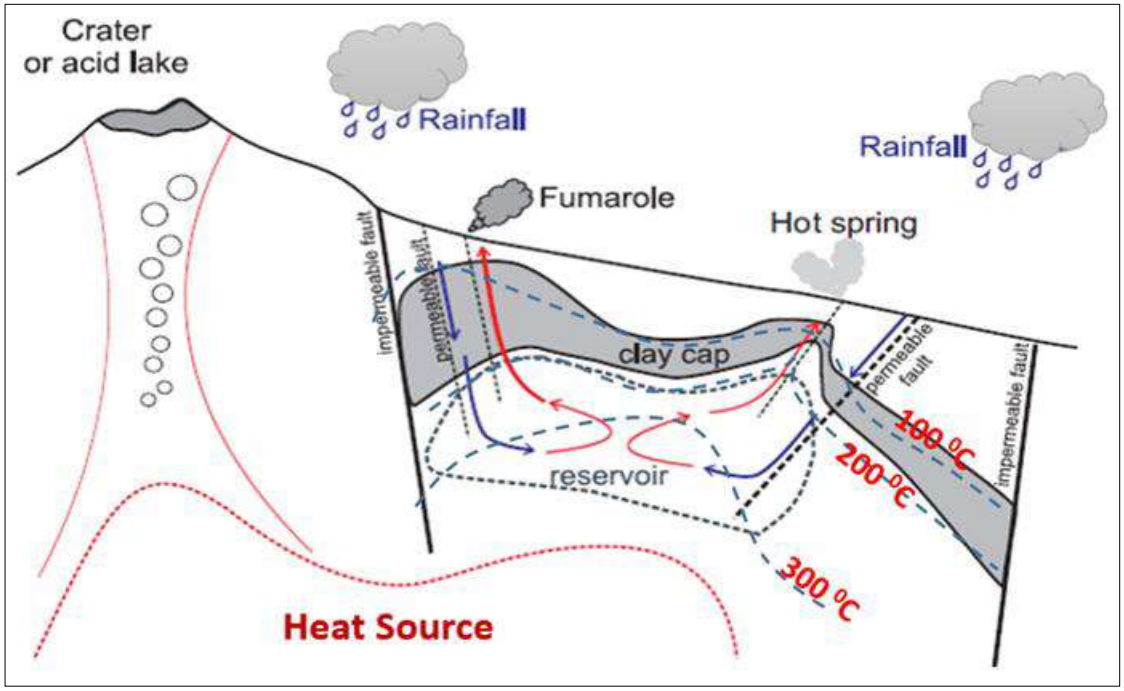

Figure 1.1: A conceptual model of a high-enthalpy geothermal system (modified from Johnston et al., 1992; Cumming & Mackie, 2007).

1.3 Location of the Study Area

The Greater Olkaria geothermal area is within the Greater Olkaria Volcanic Complex. The Olkaria Volcanic complex (Figure 1.2) lies in the Kenya's Rift Valley roughly 120 kilometers north west of Nairobi. It is bound to the north by Eburru complex, to the East and South by the Longonot and Suswa volcanoes, respectively. The rift is part of a continental divergent zone where spreading occurs resulting to the thinning of the crust hence eruption of lavas and associated volcanic activities.

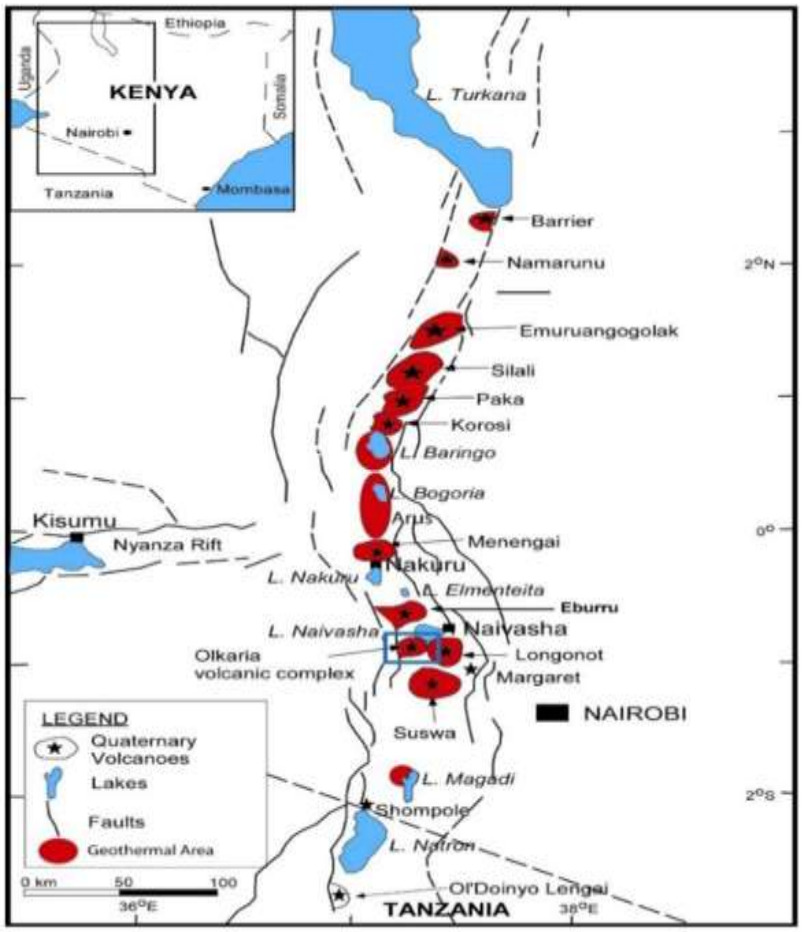

Figure 1.2: Map of Kenya showing Olkaria geothermal field (Clarke et al., 1990; Simiyu, 2010).

For geothermal development purposes, the Olkaria geothermal field is divided into seven fields: Olkaria East, Olkaria Northeast, Olkaria Central, Olkaria Northwest, Olkaria Southwest, Olkaria Southeast, and Olkaria Domes (Figure 1.3).

The greater Olkaria volcanic complex is divided into six major rock type categories: The Proterozoic basement formation, pre-Mau volcanics, Mau tuffs, plateau trachytes, Olkaria basalt and upper Olkaria volcanics (Omenda, 2000).

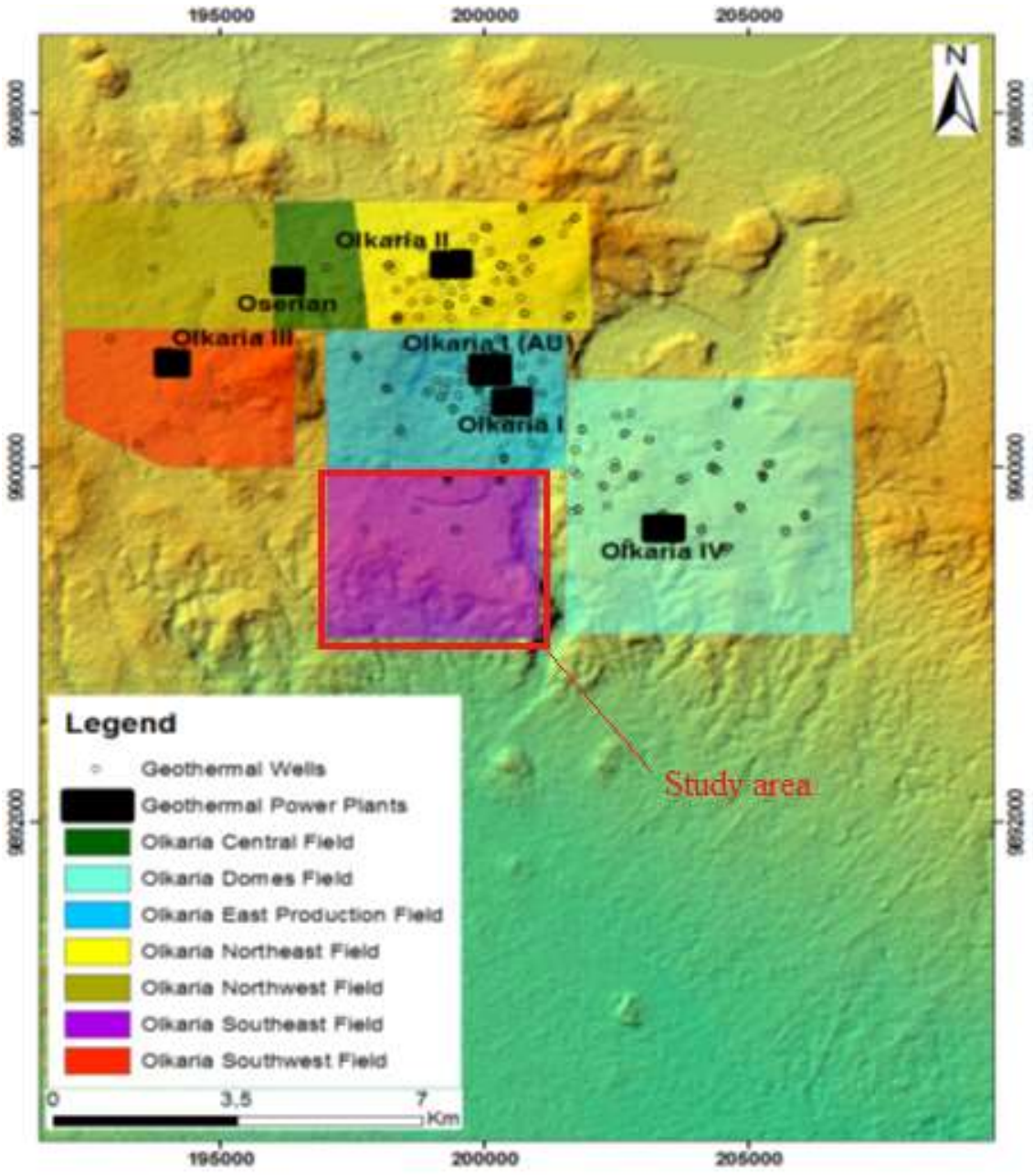

Figure 1.3: Sub-sectors of the Greater Olkaria Geothermal Field (Munyiri, 2016).

1.4 Geology of the Study Area

The Greater Olkaria Volcanic Complex (GOVC), is characterized by comendite lava flows and pyroclastics on the surface and basalts, trachytes and tuffs in the subsurface (Figure 1.4) (Clarke *et al*., 1990). Olkaria wells have plateau trachytes occurring from depth of approximately 1000m to 3000m. These trachytes often appear in conjunction with minor basalts, tuffs and rhyolites. The Olkaria basalts underlie the upper Olkaria volcanics east to the Olkaria Hill and consist of basalts with minor pyroclastics and trachytes to the west of the Olkaria Hill (Omenda, 2000).

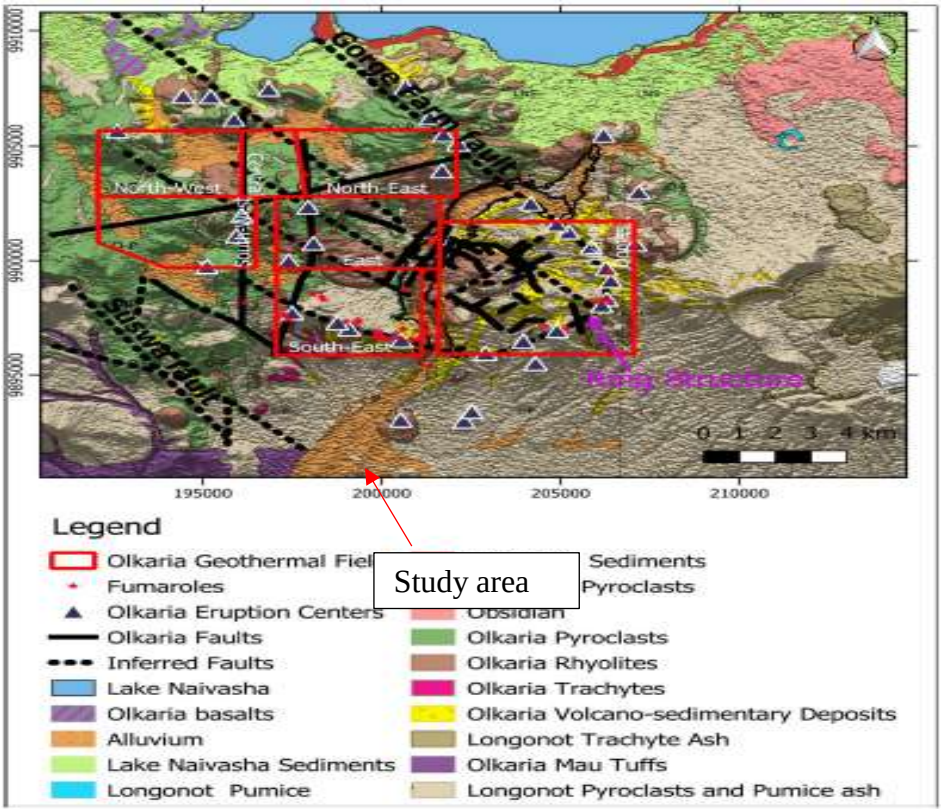

Figure 1.4: Structural and surface geological map of the Greater Olkaria Volcanic Complex (modified from Clarke et al., 1990).

1.5 Statement of the Problem

There has been less exploration done in the south east fields mainly due to community hostility, as well as unsuccessful wells drilled in the past. Drilling started in 1973 with well OW-1 located to the southeast of the greater Olkaria system (Swesco & Virkir, 1976; Ofwona, 2002). This well was drilled to a depth of 1003 m and did not discharge on its own due to low temperature and permeability. The temperature measured at 1000 m was 126°C and the water rest level was 618 m below the wellhead. The well was stimulated into production by air-lift, but it could not sustain production. The south east field has significant surface manifestation but the area also experiences temperature reversals from the data obtained from the already drilled wells. Therefore, the need for an updated conceptual model of the region to better understand deep seated structures.

2D inversion data analysis model have been used to map the subsurface resistivity. It however has limitations in mapping the deep-seated structures which are ambiguous giving inaccurate information which have been successfully solved by 3D inversion models (Uchida & Sasaki, 2006). Hence, 3D inversion was applied to the data after data processing and noise removal.

1.6 Objectives

1.6.1 General Objective

To characterize geothermal resource in the Olkaria South East field using multidimensional magnetotelluric data inversion.

1.6.2 Specific Objectives

i. To develop 1D, 2D and 3D MT models of the geothermal systems in the study area and use them to better understand its structure.
ii. To delineate the extent of the geothermal reservoir.
iii. To locate the inflow and the upflow zones from the resistivity models.

iv. To develop a revised resistivity conceptual model of Olkaria South East field.

1.7 Justification

3D MT modeling and inversion has emerged as a promising technique to model and image geothermal reservoirs in a single self-consistent manner at presumably optimal accuracy and resolution. MT method is based on induced electromagnetic fields originating outside the earth hence not affected by terrain and electrode polarization as in case of DC methods. The method is also capable of probing the subsurface from shallow to much deeper levels. The 3D resistivity models help understand the resistivity structure of the area and their characteristics. The results were also used to locate the upflow and inflow zones and help delineate the extent of the geothermal reservoir.

CHAPTER TW0

LITERATURE REVIEW

2.1 Magentotelluric Method

In Olkaria, direct current resistivity methods have been used for reconnaissance mapping, location of faults for drilling targets and to define the boundaries of geothermal reservoirs (Wamalwa *et al*., 2013). A conducted DC electric resistivity survey method revealed medium to high (30-100 Ωm) resistivity anomalies below 800 m a.s.l (above sea level) and interpreted them as intrusions associated with cooler fluids (Onancha & Mungania, 1993).

Magentotelluric (MT) and Transient Electromagnetic (TEM) are the commonest resistivity methods applied during prospecting for geothermal energy. These methods are used to measure electrical resistivity with depth. Low resistivities are generally associated with geothermal reservoirs and are due to the presence of hot rocks and saline hot waters.

Resistivity data interpretation from the Olkaria geothermal field shows that the low resistivity (less than 20 Ωm) anomalies at depths of 1000 meters above sea level that define the geothermal resource boundaries are controlled by linear structures in the NE-SW and NW-SE directions (Mulwa & Mariita, 2013, 2015; Wamalwa & Serpa, 2013; Ofwona, 2008; Abdelfettah *et al*., 2016,). Some of the high resistivity regions coincide with recharge areas associated with NE and NW trending faults that act as conduits for cold water flow from the Rift Valley scarps. The geothermal fluid up-flow zones occur at the intersections of these regional faults in the vicinity of a heat source.

1D TEM and MT inversion carried out revealed Olkaria geothermal field is characterized by a thin shallow layer of high resistivity on the surface especially on higher grounds. This was interpreted as unaltered rock formations on the surface possibly due to the thick pyroclastic cover. Below it is a low resistivity (< 15 Ωm) layer that extend to approximately 1000 meters above sea level. This layer is presumed to be dominated by

low temperature alteration minerals such as smectite and zeolite and defines the clay cap. A deep high resistivity (resistivity core) layer with values greater than 100 Ωm is observed underlying the clay cap. This is a zone where high temperature hydrothermal alteration minerals such as epidote, chlorite and actinolite are observed and is interpreted as the reservoir zone (Wanjohi, 2014).

The joint 1D inversion method has been the primary data MT analysis and interpretation technique applied in the Olkaria field (Lichoro, 2010; Mwangi, 2018). They mapped anomalously high and low resistivity bodies in the study area. However, the lateral resolution of geological structures was limited.

Mwangi *et al*. (2008) performed a dimensionality analysis of the Olkaria geothermal field. The dimensionality analysis showed the data is 3D and this is supported by the 3D nature of the underlying major structures.

Because the Earth is 3D, a 2D Earth model cannot be used to accurately explain or represent the 3D Earth and it will be based on assumptions. If the data contains 3D structures, 2D inversion can mislead an interpretation.

2.2 Theoretical Background

This section details with the theoretical background of the methodologies used.

2.2.1 The Theory of Magentotelluric

MT method is a passive, frequency domain electromagnetic method which uses electric and magnetic field variations of natural origin (Vozoff, 1991). When this external energy, known as the primary electromagnetic field, reaches the earth's surface, part of it is reflected back and remaining part penetrates into the earth. Earth acts as a good conductor, thus electric currents (known as telluric currents) are induced in turn to produce a secondary magnetic field.

On the earth's surface, fluctuations in the natural magnetic field B and the induced electric field E are measured. The electrical properties such as electrical conductivity of the underlying material can be determined from the relationship between the components of the measured electric (E) and magnetic field (B) variations, or transfer functions: The horizontal electric (Ex and Ey) and horizontal (Bx and By) and vertical (Bz) magnetic field components (Naidu, 2012). The basic MT response, Z, can be defined as the linear relationship between horizontal electric and magnetic field variations at a specific station at the Earth's surface. Z, also known as the impedance tensor, is frequency dependent and contains the information about the subsurface conductivity structures (Cagniard, 1953). Since low frequency signals are sensitive to the earth's lower layers and high frequency signals give information about the shallow surface, the variation of electrical resistivity with depth can be detected utilizing a wide frequency range.

2.2.2 Sources of MT

Natural electromagnetic (EM) signals are generated from two source which are: At the lower frequencies, generally less than 1 Hz, or more than 1 cycle per second, and the high frequency signal greater than 1 Hz or less than 1 cycle per second.

The lower frequency signal originates from the interaction of the solar wind with the earth's magnetic field. Solar wind is a stream of plasma mostly ions, electrons and protons radiating continually from the sun (Parker, 1958).

High frequency EM signals originate from world-wide thunderstorm activity, usually near the equator. The signals discharged from the lightning are known as 'sferics'. They propagate to great distances and contains a broad range of EM frequencies (Simpson & Bahr, 2005).

The above signal sources create a measurable time varying electromagnetic wave (Tikhonov, 1950; Cagniard, 1953).

2.2.3 Electromagnetic Properties of the Earth

Since MT is an EM method, the rock properties of interest describing the behavior of a medium in relation to the penetration of EM fields are the material specific electric and magnetic properties.

Electrical properties

Electrical properties of a material are descried by conductivity, σ or resistivity, ρ which is the inverse of conductivity and the electrical permittivity, ε. The electrical conductivity measures the ability of a material to conduct an electrical current. While conductivity is a rock and mineral property, its variation does not only depend on the composition and rock type, but also the overall physical condition of the medium such as temperature, and presence of fluids. Presence of highly conduction minerals such as graphite can also affect conductivity. Figure 2.1 below shows ranges of resistivities of rocks.

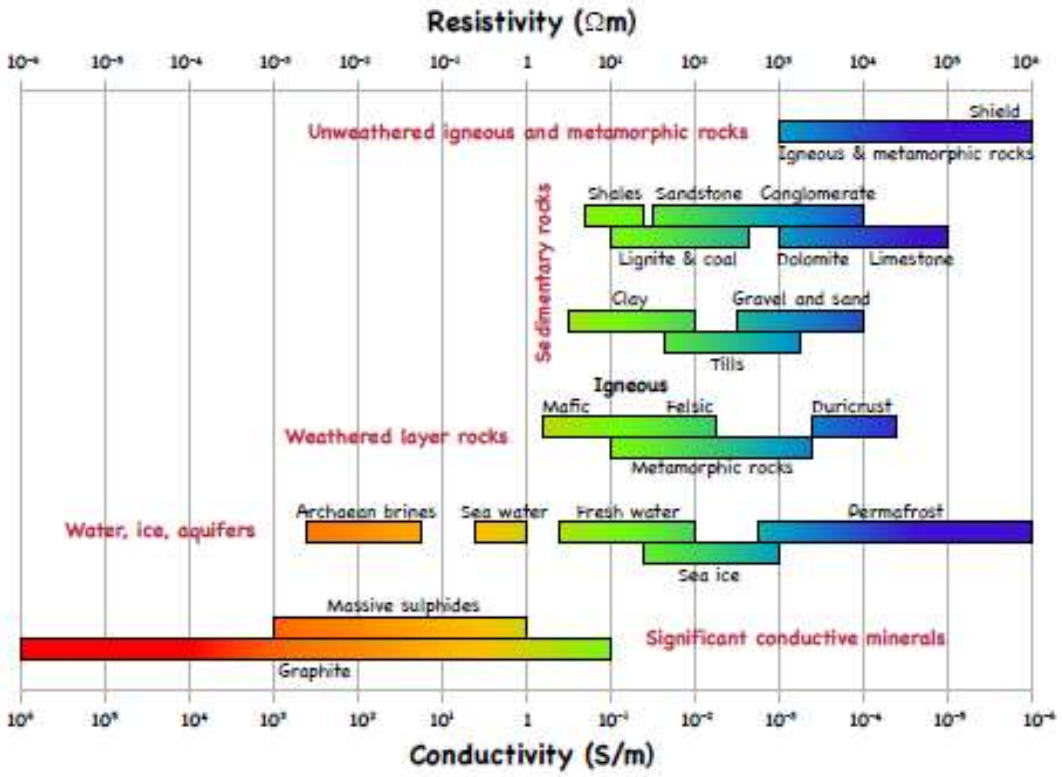

Figure 2.1: Ranges in electrical conductivity and resistivity common Earth materials (Marti, 2006; Palacky, 1988).

From the ohms law current density relates to the electrical field as shown:

$$\hat{j} = \sigma \hat{E} \qquad \textbf{(0.1)}$$

Where $\hat{j}$ is the current density, σ is the conductivity and $\hat{E}$ is the electrical field.

Electrical permittivity describes how an electric field affects and is affected by a dielectric medium. It's a measure of the material's ability to become polarized by an external electric field. Permittivity describes the material's nature of transmitting electric fields (Simpson & Bahr, 2005).

The relation between electrical displacement $\hat{D}$ and electrical field $\hat{E}$ is given as:

$$\widehat{D} = \varepsilon \widehat{E} \quad (0.2)$$

Where ε is the electrical permittivity.

Magnetic properties

Magnetic permeability μ is the degree of magnetization of a material that responds linearly to an applied magnetic field (Griffiths, 1999). The relationship between magnetic induction, $\widehat{B}$ and magnetic intensity, $\widehat{H}$ is as given below:

$$\widehat{\boldsymbol{B}} = \boldsymbol{\mu}\widehat{\boldsymbol{H}} \quad (0.3)$$

2.2.4 Assumptions of the MT Method

MT method assumes:

i. The maxwells equations as described in section 2.2.5 are obeyed.
ii. Earth does not generate electromagnetic energy; it only absorbs or dissipates it.
iii. EM source fields may be treated as uniform plane-polarized EM waves which are generated at a relatively distant source and have a near-vertical angle of incidence to the earth's surface.
iv. The earth acts as an ohmic conductor and the charges are conserved.
v. For the period range used in MT usually 10^{-5} to 10^{5} s, the time varying displacement currents are small compared to the time varying conduction currents and may be neglected.
vi. Variations in the electrical permittivities and magnetic permeabilities of rocks and minerals are negligible compared with variations in the bulk rock conductivities.

2.2.5 Maxwell's Equations

The fundamental equations governing the behavior of electromagnetic fields are given by Maxwell's equations (Maxwel, 1865):

$$\nabla \times B = \mu\sigma E + \mu\varepsilon \frac{\partial E}{\partial t} \quad \text{(Ampere's law)} \tag{0.4}$$

$$\nabla \times E = -\frac{\partial B}{\partial t} \quad \text{(Faraday's law of induction)} \tag{0.5}$$

$$\nabla \cdot B = 0 \quad \text{(Gauss's law for magnetism)} \tag{0.6}$$

$$\nabla \cdot E = \frac{\eta}{\varepsilon} \quad \text{(Gauss's Law)} \tag{0.7}$$

Where E is the electric field, B is the magnetic flux density and η is the electric charge density owing to free charges, ε is the electric permittivity of free space, σ is the conductivity, μ magnetic permeability and t is time.

consider vector calculus identity given by equation 2.8,

$$\boldsymbol{\nabla} \times (\boldsymbol{\nabla} \times \boldsymbol{A}) = \boldsymbol{\nabla} \cdot (\boldsymbol{\nabla A}) = \boldsymbol{\nabla}(\boldsymbol{\nabla} \cdot \boldsymbol{A}) - \boldsymbol{\nabla^2 A} \tag{0.8}$$

Where A is a vector quantity and assuming there are no free charges (η = 0) then, $\nabla \cdot E = 0$, and taking curl of equation 2.5 and substituting it in equation 2.4 we get equation 2.9

$$\nabla^2 E = \mu\sigma \frac{\partial E}{\partial t} + \mu\varepsilon \frac{\partial^2 E}{\partial t^2} \tag{0.9}$$

The first term gives conduction current and the second term gives displacement current (Simpson & Bahr, 2005).

The homogeneous earth

For an isotropic and homogeneous space, the conductivity is constant. Assuming a plane wave with a harmonic time dependence of the form $e^{-i\omega t}$ and neglecting displacement current, equation 2.9 can be simplified as:

$$\nabla^2 E = i\mu\omega\sigma E \qquad (0.10)$$

Where ω is the angular frequency defined as $\omega = 2\pi f$. Where f is the frequency and reciprocal of period T(s) (Simpson & Bahr, 2005). Equation 2.10 above is known as Helmholtz equation which has a wave number = $\sqrt{-i\mu\omega\sigma}$ and a solution as $\nabla^2 E = E_o e^{kz}$.

2.2.6 Skin Depth

As electromagnetic fields diffuse into a medium, they decay exponentially, this is the principle of skin depth.

Considering the real part of the Helmholtz equation (equation 2.10) and using

$$\sqrt{-i} = \sqrt{\frac{1}{2}} - \sqrt{\frac{i}{2}} \qquad (0.11)$$

Skin depth can be expressed as:

$$\delta = \sqrt{\frac{2}{\mu_o \omega \sigma}} = \sqrt{\frac{1}{\mu_o \pi f \sigma}} = \sqrt{\frac{\rho T}{\mu_o \pi}} \quad (0.12)$$

where δ is the electromagnetic skin depth in meters at a given period T, σ is the conductivity of the medium penetrated, μ is the magnetic permeability and ρ is the resistivity. If we assume a free space value for magnetic permeability, then skin depth can be expressed as:

$$\delta \cong 503\sqrt{\rho T} \quad (0.13)$$

Therefore, in MT, one electromagnetic skin depth is generally equated to the penetrating depth of the electromagnetic fields into the earth.

The electromagnetic fields are attenuated to e^{-1} of their amplitudes at the surface of the earth, at a depth δ. This exponential decay of electromagnetic field with increasing depth renders them insensitive to deeper lying conductivity structure than δ (Griffiths, 1999).

Therefore, at a zeroth order conceptual level, magentotelluric comprises measurements of the skin depth as a function of period to infer resistivity as a function of position in earth.

2.2.7 Magentotelluric Transfer Functions

MT transfer functions or MT responses are functions that relate the registered electromagnetic field components at given frequencies. MT responses only depend on the electrical properties of the material and not the electromagnetic source. Therefore, they characterize the conductivity distribution of the underlying materials according to the measured frequency. They include:

Impedance Tensor

Impedance tensor is the relation between orthogonal electric (E_x, E_y) and magnetic (H_x, H_y) fields at a given frequency. It is described by the equation below which can be expressed in a matrix form as:

$$\begin{bmatrix} \boldsymbol{E_x} \\ \boldsymbol{E_y} \end{bmatrix} = \begin{bmatrix} \boldsymbol{Z_{xx}} & \boldsymbol{Z_{xy}} \\ \boldsymbol{Z_{yx}} & \boldsymbol{Z_{yy}} \end{bmatrix} \begin{bmatrix} \boldsymbol{H_x} \\ \boldsymbol{H_y} \end{bmatrix} \tag{0.14}$$

The impedance Z is a complex tensor and is a function of the earth's resistivity ρ. The asymmetry of the material is given by on-diagonal components of Z. They become zero if the material is symmetric about a vertical plane passing through the observation site (Berdichevsky and Dmitriev, 2002). The off-diagonal components of Z give the information about vertical variations in resistivity structure. The complexity of the impedance tensor is dependent on the dimensionality of the subsurface medium. In the 1D and 2D case there are a few simplifications that become invalid once the complexity of the structure increases.

Geomagnetic Transfer Functions (Tipper Vector)

The geomagnetic transfer function T describes the relationship between the horizontal and the vertical magnetic field components expressed as:

$$\boldsymbol{H_z} = (\boldsymbol{T_x}, \boldsymbol{T_y}). \begin{pmatrix} \boldsymbol{H_x} \\ \boldsymbol{H_y} \end{pmatrix} \tag{0.15}$$

Geomagnetic transfer function is a complex frequency dependent vector. Induction arrows are the commonly used to represent this vector (Parkinson, 1959 & Weise, 1962).

They are two real and dimensionless vectors:

$$\boldsymbol{T_{Re}} = \left(\boldsymbol{R_e T_x}, \boldsymbol{R_e T_y}\right) \tag{0.16}$$

And

$$\boldsymbol{T_{Im}} = \left(\boldsymbol{I_m T_x}, \boldsymbol{I_m T_y}\right) \tag{0.17}$$

Which represent the real and the imaginary parts on an x-y plane. Induction arrows can be used to indicate the lateral variations of conductivity since vertical magnetic fields are generated by lateral conductivity gradients. There are two conventions for plotting the induction arrows:

Parkinson convention- The vectors point towards the increase in lateral conductivity. Arrows have real(in-phase) and quadratic(out-of-phase) parts. The length of the real part is given as:

$$\left(-\boldsymbol{R_e T_x i} - \boldsymbol{R_e T_y j}\right) \tag{0.18}$$

And the quadratic part is given as:

$$\left(\boldsymbol{I_m T_x i} + \boldsymbol{I_m T_y}\,\mathbf{j}\right) \tag{0.19}$$

where i, j are the Cartesian unit vectors towards magnetic north and east, respectively.

Weise convention- the vector points away from the lateral increase in electrical conductivity. The induction arrow of the real part is given by:

$$\left(\boldsymbol{R_e T_x^2 + R_e T_y^2}\right)^{1/2} \tag{0.20}$$

and an angle

$$\tan^{-1} \frac{\boldsymbol{R_e T_y}}{\boldsymbol{R_e T_x}} \tag{0.21}$$

Whereas the magnitude of the imaginary part is given by:

$$\left(\boldsymbol{I_m T_x^2 + I_m T_y^2}\right)^{1/2} \tag{0.22}$$

And an angle

$$\tan^{-1} \frac{\boldsymbol{I_m T_y}}{\boldsymbol{I_m T_x}} \tag{0.23}$$

The angles show the orientation of the arrows, clockwise position from x- direction (usually geomagnetic north).

2.2.8 The Dimensionality of the Subsurface Structure

The 1D Earth

For the simple case of a 1D, isotropic layered Earth (i.e., the conductivity changes only with depth) the diagonal components (Z_{xx} and Z_{yy}) of the impedance tensor, which are related to the parallel electric and magnetic fields, are zero. Since there is no lateral conductivity variation, the off-diagonal elements ($Z_{xy}$and Z_{yx}) have the same amplitude, but are of different sign and can be written as follows:

$$\boldsymbol{Z_{1D}} = \begin{pmatrix} \mathbf{0} & \boldsymbol{Z_{xy}} \\ \boldsymbol{Z_{yx}} & \mathbf{0} \end{pmatrix} = \begin{pmatrix} \mathbf{0} & \boldsymbol{Z_{xy}} \\ -\boldsymbol{Z_{xy}} & \mathbf{0} \end{pmatrix} \tag{0.24}$$

The corresponding apparent resistivity is given by:

$$\boldsymbol{\rho_a} = \frac{\mathbf{1}}{\boldsymbol{\mu\omega}} \mathbf{|Z|^2} \tag{0.25}$$

Where ρ_a is the apparent resistivity defined as the average resistivity of an equivalent homogeneous half space. And the impedance phase, is given by:

$$\emptyset_{\mathbf{a}} = \mathbf{tan^{-1}} \frac{\mathbf{I_m Z}}{\mathbf{R_e Z}} \tag{0.26}$$

The 2D Earth

In a 2D Earth, resistivity varies with depth and also in one of the horizontal directions (for instance, along a profile). The direction of constant resistivity is known as geoelectric strike direction.

The impedance tensor can be written as follows:

$$Z_{2D} = \begin{pmatrix} 0 & Z_{xy} \\ Z_{yx} & 0 \end{pmatrix} = \begin{pmatrix} 0 & Z_{TE} \\ Z_{TM} & 0 \end{pmatrix} \quad (0.27)$$

The rotation of Z involves the decomposition of the electric and magnetic field components into E-polarization (TE mode) and B-polarization (TM mode) (Berdichevsky & Dmitriev 2008).

In the TE mode the electric field is aligned with the electric strike and in the TM mode the magnetic field is aligned with the strike as shown in figure 2.2. If x-axis is in the strike direction, the off-diagonal components become:

$$\rho_{xy} = \frac{1}{\omega\mu_0}|Z_{xy}|^2 \qquad \text{TE mode} \quad (0.28)$$

$$\rho_{yx} = \frac{1}{\omega\mu_0}|Z_{yx}|^2 \qquad \text{TM mode} \quad (0.29)$$

Where ω is the angular frequency and $\mu_0$is permeability of free space.

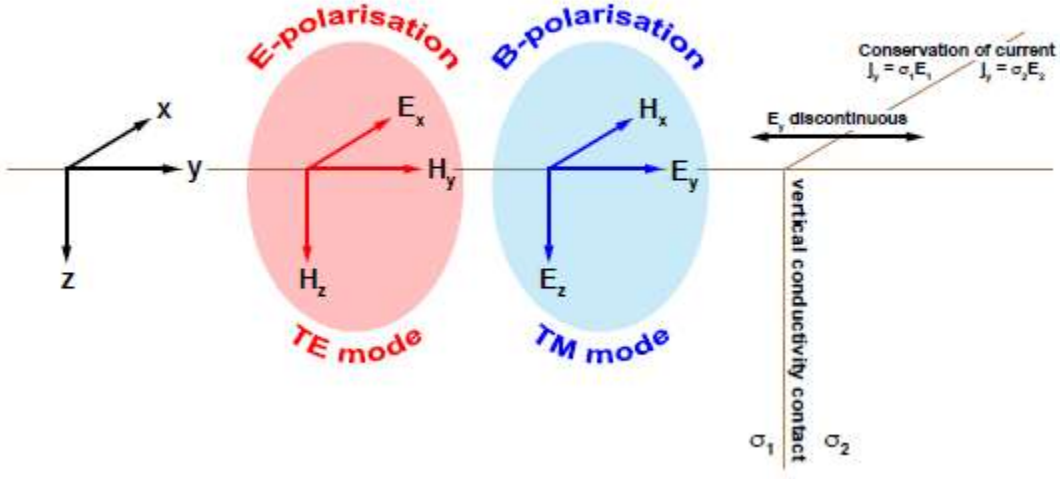

Figure 2.2: A simple model for the ideal 2D case showing TE and TM modes. Redrawn and modified from Simpson and Bahr (2005).

The 3D Earth

In the 3D earth, conductivity distribution varies with depth and in both lateral directions. The impedance tensor is expressed as:

$$Z_{3D} = \begin{pmatrix} Z_{xx} & Z_{xy} \\ Z_{yx} & Z_{yy} \end{pmatrix} \tag{0.30}$$

Methods used in dimensionality analysis are as discussed below:

Skew

Skew is the ratio of diagonal components to the off-diagonal components.

$$\boldsymbol{swift_{skew}} = \left| \frac{\boldsymbol{Z_{xx} + Z_{yy}}}{\boldsymbol{Z_{xy} - Z_{yx}}} \right| \tag{0.31}$$

If the values of skew are > 0.3 it has 3D characteristic, if skew <0.3 it has 1D or 2D structures (Pranata *et al*., 2017).

Bahr Skew

Bahr skew is also known as phase sensitive or regional skew. It is a measure of the skew of phases of the impedance tensor. Unlike swift skew and ellipticity Bahr skew is not affected by distortion and it is defined by:

$$\eta = \frac{|[D_1,\ S_2] - [S_1, D_2\ ]|^{1/2}}{|D_2|} \qquad (0.32)$$

Where η is the Bahr's skew and $S_1 = Z_{xx} + Z_{yy}$, $S_2 = Z_{xy} + Z_{yx}$, $D_1 = Z_{xx} - Z_{yy}$, $D_2 = Z_{xy} - Z_{yx}$.

If the skew value is < 0.1 it indicates 1D or 2D, if 0.1 > skew > 0.3 it indicates 2D or 3D and if skew is > 0.3 it indicates 3D.

Ellipticity

Ellipticity is calculated using the equation:

$$\boldsymbol{Ellipticity} = \frac{\boldsymbol{Z'_{xx} - Z'_{yy}}}{\boldsymbol{Z'_{xy} + Z'_{yx}}} \qquad (0.33)$$

Z' denotes rotated impedance tensor, x and y represent orthogonal directions in a coordinate system. This quantity is limited as a dimensionality indicator because at places where $Z'_{xx} = Z'_{yy}$, the fields could be influenced by an anomaly and require a 3D resistivity structure in order to describe their variation. This has been shown to be true especially at low frequencies. This deficiency can be offset by calculating skew, which increases at low frequencies where the impedance tensor is affected by a larger volume of

the earth. Impedance ellipticity is useful in determining the response, and hence the structural dimensionality at a site (Ranganayaki, 1984).

Phase Tensor

Dimensionality evaluated using phase tensor gives the best results by considering MT sites from different locations collectively. Phase tensor provides the better solution for dimensionality and strike direction and is not affected by galvanic distortion. The phase tensor Φ is defined as the ratio of the real (X) and imaginary parts (Y) of the complex impedance tensor, Z.

$$\Phi = Y/X \tag{0.34}$$

Where,

$$Z = X + Iy \tag{0.35}$$

The phase tensor can be illustrated graphically (Figure 2.3) by an ellipse with skew angle (β) and minimum (Φ_{min}) and maximum (Φ_{max}) principal axes. The skew angles in phase tensor maps, is mostly represented as colour filling of the ellipses. The phase tensor can be expressed in terms of α, β, Φ_{min} and Φ_{max} as follows:

$$\Phi = R^{T}(\alpha - \beta)\begin{bmatrix}\Phi max & 0\\ 0 & \Phi min\end{bmatrix}R(\alpha + \beta) \tag{0.36}$$

where $\boldsymbol{R}$ (α+ β) is the rotation matrix and $\boldsymbol{R}^{T}$ is inverse rotation matrix. The strike of the major axis of the ellipse is given by α − β, and in the case of a 2D or 3D/2D Earth, β is zero and the 2-D strike direction is given by α.

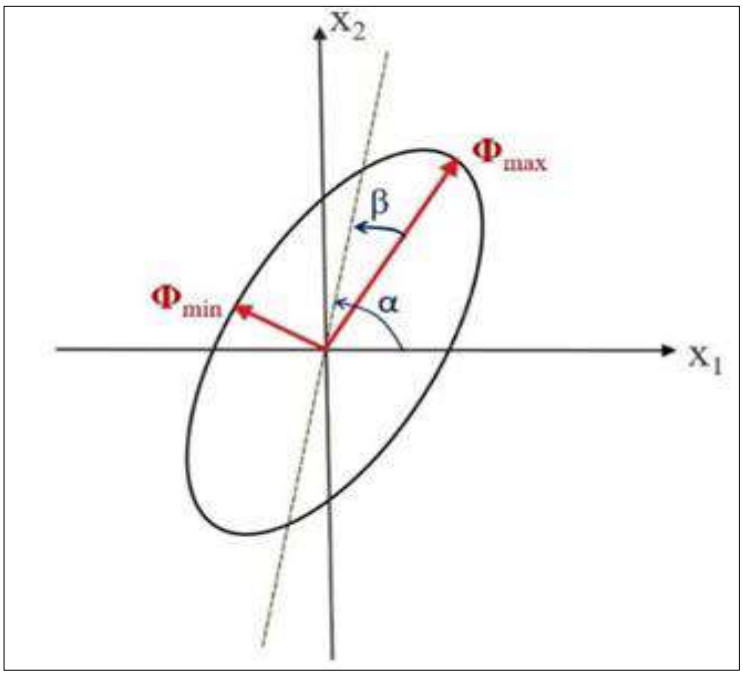

Figure 2.3: Phase tensor graphic representation (Caldwell et al., 2004).

If the phase tensor is non-symmetrical, the skew angle β, is required as a third coordinate invariant to characterize the tensor. The relationship between the tensor and the observational reference frame (x1 and x2) is defined by the angle α - β, which determines the orientation of the principal axis of the ellipse.

For 1D case, the phase tensor is characterized by a small skew angle and a circular shape. Naturally, if the conductivity is both isotropic and 1D, the radius of the circle will vary with frequency according to the variation of the conductivity with depth. The radius will increase if the conductivity increases with depth. For a 2D regional resistivity structure, β becomes zero for noise free data and close to zero for field data and phase tensor will be represented by an ellipse. In the presence of 3D structure, the phase tensor is non-symmetric and has a large skew angle (β) value. Phase tensor ellipses maps at different

frequency provide a simple way of visualizing lateral changes in the regional conductivity structure at different depths. Such maps will not be influenced by near-surface galvanic effects (Caldwell *et al*., 2004).

2.2.9 The Galvanic Distortion

Distortion in MT is produced by shallow and low bodies or heterogeneities which are much smaller compared to the targets of interest and skin depth. These bodies cause charge distribution and induced currents that alter the magentotelluric responses at regional scale (Keller, 1983). Distortions can either be induced or galvanic. Induced distortion is generated by current distributions. It has a small magnitude and decays with the period. Under the condition $\sigma \gg \omega\varepsilon$ it can be ignored. Where σ is conductivity, ω is the angular frequency and ε is the electric permittivity (Berdichesky & Dmitriev, 2002).

2.2.10 Static Shift

In cases of 1D regional earth galvanic distortion produces a constant displacement of the apparent resistivity along all frequencies and this is known as static shift. Since the magnetic field is relatively unaffected by static shift, a controlled source magnetic field sounding such as TEM can be used to correct for static shift. Static shift correction of the data was done using spatial median filter method. This method estimates the median of each polarization of the apparent resistivity for stations within a given radius and is compared to each station within the same radius for a given period range. If the difference is greater than a given tolerance, then that difference is assumed to be a static shift and is removed from the two components of the impedance for that polarization (Berdichesky & Dmitriev, 2008).

2.2.11 Occam's and ModEM Inversion Codes

Forward modelling codes for MT data are available for 1D, 2D and 3D cases, while in the inversion case mainly 1D and 2D codes are available for standard applications such as, REBOCC by Siripunvaraporn and Egbert (2000), OCCAM 1D and 2D by Constable *et al.*

(1987) and RLM2DI by Rodi and Mackie (2001). A number of 3D inversion codes has grown in recent years, for example WSINV3DMT code (Siripunvaraporn *et al*., 2004), ModEM code developed by Egbert and Kelbert (2012), Meqbel (2009) and Kelbert *et al.* (2014), have become freely available for the purpose of research. In this study OCCAM'S code was used for1D and 2D inversion and ModEM code for 3D inversion.

The advantage of the Occam's code is its ability to converge in a small number of iterations. In addition, because it searches for the minimum structure model, the model can be treated as a "lower bound" for interpretation indicating the structures that are required by the data (Constable *et al*., 1987). Similarly, ModEM algorithm requires a small amount of memory usage as it avoids explicitly computing and storing Jacobian matrix.

1D Inversion

1D inversion assumes resistivity varies with depth only. Occam inversion was used for 1D inversion in Olkaria South East field. The program was developed by the Scripps Institute of Oceanography (Key, 2011). and is based on the minimization of the following unconstrained regularized functional (Constable et al., 1987):

$$U = \|\partial m\|^2 + \|P(m - m_*)\|^2 + U^{-1}\left\{\left\|W\left(d - F(m)\right)\right\|^2 - X^2,,\right\} \quad (0.37)$$

The first term represents the norm of the model roughness, the second term is the model update and the term $d - F(m)$ represents the data misfit between the observed d and the predicted response $F(m)$. W is the data covariance weighting function which is a diagonal matrix with elements corresponding to inverse data standard errors. U^{-1} is the Lagrange multiplier which balances the trade-off between the data fit and the model roughness and model preference. X^2 is the target misfit, chosen so that root mean square is equal to unity.

2D inversion

2D inversion assumes that the resistivity varies with depth and in one lateral direction and that the resistivity is constant in the other horizontal direction (electrical strike).

Occam's 2D inversion code (version 3.0) developed by Scripps Institution of Oceanography based on deGroot-Hedlin and Constable (1990) was used for this study. Occam's 2D inversion is based on the minimization of the following unconstrained functional:

$$\boldsymbol{U = \left\|d_y m\right\|^2 + \|d_z m\|^2 + U^{-1}\left\{\left\|W\left(d - F(m)\right)\right\|^2 - X^2,,\right\}} \qquad (0.38)$$

where the expression, $\left\|d_y m\right\|^2 + \|d_z m\|^2$ is the norm of the model roughness, U^{-1} represents the Lagrange multiplier, the third term in the equation represents the data misfit, W is M x M diagonal weighting matrix, d represents the observation vector, F(m) is the model response and the last term X^2 is the target misfit.

Transverse electric (TE) mode and transverse magnetic (TM) mode

The 2D magnetotelluric field consists of two modes that is the TE and TM modes. The TM mode is related to the B-polarized wave generating the transverse MT curves (telluric current flows across the structures), and the TE mode is related to the E-polarized wave generating soundings MT curves (telluric current flows along the structures).

TM mode charges the structures and its anomalies galvanic in nature. TE on the other hand does not charge the structures and its anomalies are of inductive nature. The TM and TE modes offer different sensitivities to near-surface and deep structures and provide different accuracies of 2D approximation of real 3D bodies (Berdichevsky *et al.*, 1998).

3D Inversion

ModEM code developed by Egbert and Kelbert (2012), Meqbel (2009) and Kelbert et al. (2014) will be used to analyze the MT data to produce a 3D resistivity model consistent with MT data that require it. The 3D inversion implemented in ModEM code is based on the minimization of the following penalty functional:

$$\boldsymbol{U(m,d) = \big(d - F(m)\big)^T C_d^{-1}\big(d - F(m)\big)} \\ \boldsymbol{+ \lambda(m - m_0)^T C_m^{-1}(m - m_0)} \tag{0.39}$$

The equation's first term represents the data misfit between the measured (d) and model response, F(m). The second term describes the model update between the estimated model (m) and initial model (m_0). λ is the regularization parameter, Cd and C_m are the data and model covariance's, respectively. In ModEM, the non-linear conjugate gradient (NLCG) approach is used to minimize the penalty function. The initial model, m_0 is updated iteratively by line search strategy and the 3D forward problem is based on the finite difference method (FDM).

CHAPTER THREE

METHODOLOGY

3.1 Materials and Methods

The equipment used include:

a. MT unit (MTU-5A) data recorder
b. Magnetic Coils
c. Electrical ports
d. Global Positioning System (GPS)
e. 12 V battery

The MT data was collected in 2021 with additional to secondary data collected by KenGen staff in 2010 and 2013 using the Phoenix MTU-5 instruments. This study used a total of 23 soundings which are distributed as shown in Figure 3.2. The MT unit consists of a data logger which records data, global positioning system (GPS) which provides the geographical coordinate and continuous time signal, essential for recording time series.

Fluctuations in the magnetic field components were measured using three magnetic coils (Hx, Hy, and Hz). The four electric ports were used to record variation of horizontal electric field and were oriented in N-S and E-W directions. The distance between each pair of electrodes (Ex and Ey) was 60 m. To ensure good conductivity the electrodes were soaked in a sodium chloride solution.

The three magnetic coils were buried at a depth of one foot and oriented as shown in Figure 3.1. The four electric ports were also buried shallowly with a solution of bentonite. The car battery was used to power the system. The distance between the electrodes was approximately 60 m. At each station, the total variation of electric in the magnetic field was recorded for about 18 hours to collect data for long periods and also take advantage of the strong signals usually available in the late hours of the night.

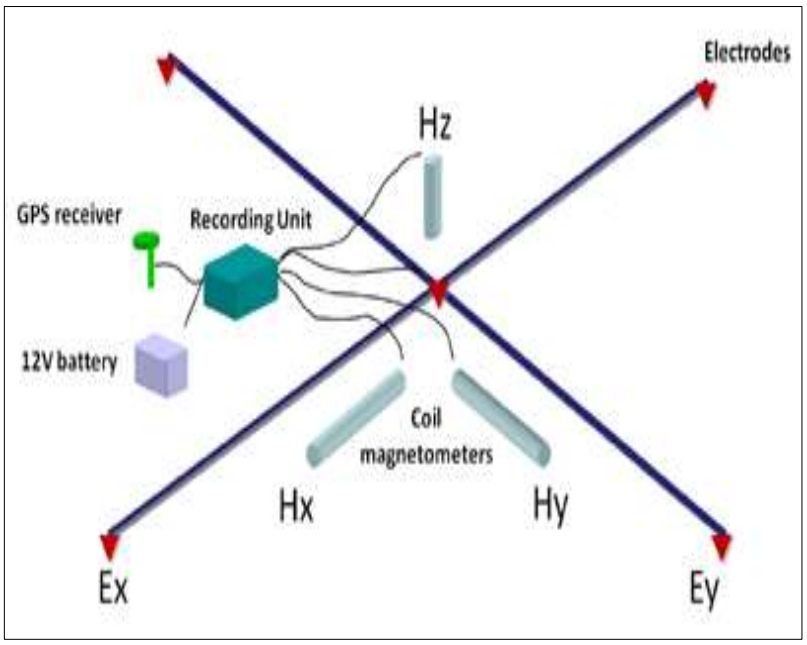

Figure 3.1: A Typical MT field set-up (Hersir and Árnason, 2009).

3.2 Data Processing

Time series data was downloaded from the MT unit using SSMT2000 program. The data was then preconditioned where severe noise was removed and then processed using Fourier Transform to transform them into frequency domain expression in terms of apparent resistivities and phase of impedance, as a function of frequency for each station in the MT Editor program provided by phoenix Geophysics- Canada. From the Fourier transform band the robust processing method was used to compute average cross power and auto power. The data was then saved in the Electronic Data Interchange (EDI) files.

3.3 1D Inversion

An initial model with 40 layers was used with the resistivity of the first layer set to 40 Ωm. The first layer thickness was set at 20 m which was increased logarithmically with

an increasing factor of 1.1 up to 5km. The maximum number of iterations was 20 with a target depth of 3km. A Lagrange multiplier of 5 was used.

3.4 2D Inversion

The profiles were cut perpendicular to the geological structures. For each profile, a mesh with a block width set to 50 m and 70 layers with an initial layer of 20 m thickness increasing logarithmically with depth was generated. An initial model of 50 Ωm homogenous half-space was used. A maximum of 100 iterations and a target root mean square of 0.5 was used with a maximum of 80 frequencies ranging from 0.011 Hz to 320 Hz. Figure 3.2 below shows the profiles taken for the MT data in south East field.

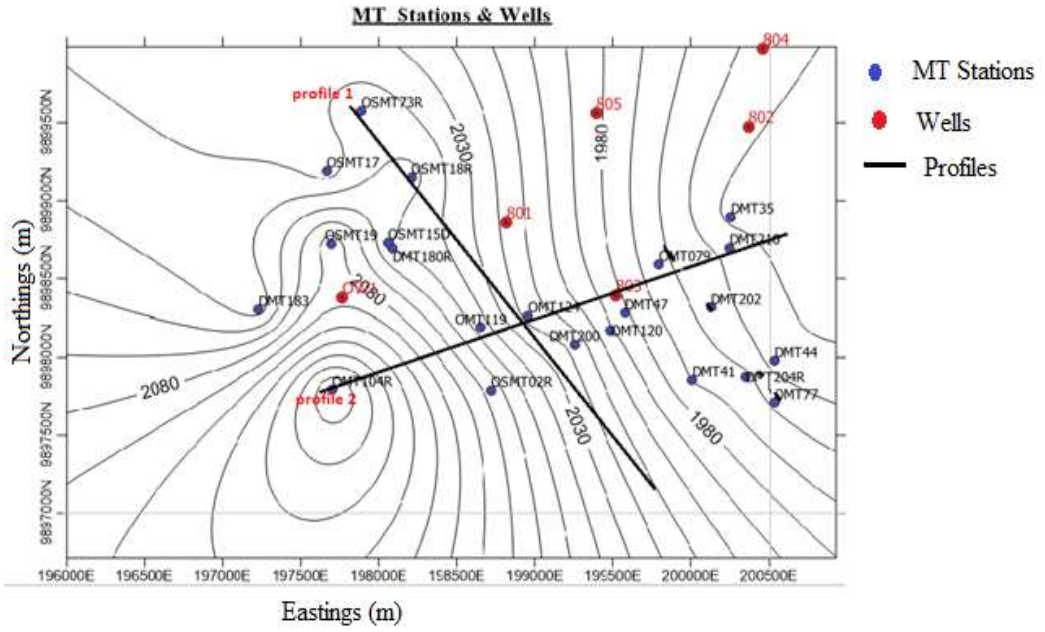

Figure 3.2: Contour map showing MT stations, wells and profiles cut.

3.5 3D Inversion

A total of 23 MT stations were used for the 3D inversion. 50 layers were used with the first layer having a thickness of 10m and they increased with an increasing factor of 1.1. The resultant model is 5km deep with 38 * 50*50 cells in x, y and z directions respectively

as shown in figure 3.3. ModEM achieved 93 iterations with a minimum root mean square misfit of 5.48.

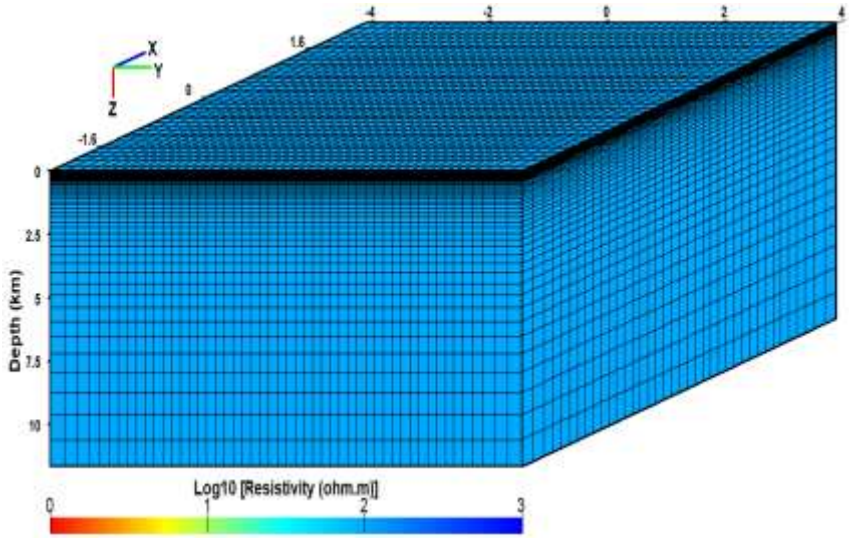

Figure 3.3: Grid model of the area.

CHAPTER FOUR

RESULTS AND DISCUSSION

This section details the results and findings of some of the stations for static shift, dimensionality and 1D inversion. Any result that is not presented in this chapter has been attached in the appendix.

4.1 Static Shift Correction

A diameter of 2km was applied to the sites which showed a significant split in the apparent resistivity curves at high frequency. The ModEM program accounted for the remaining static shift effects by introducing a scattered conductivity distribution in the near-surface layers. Figure 4.1 shows curves before and after static shift was done.

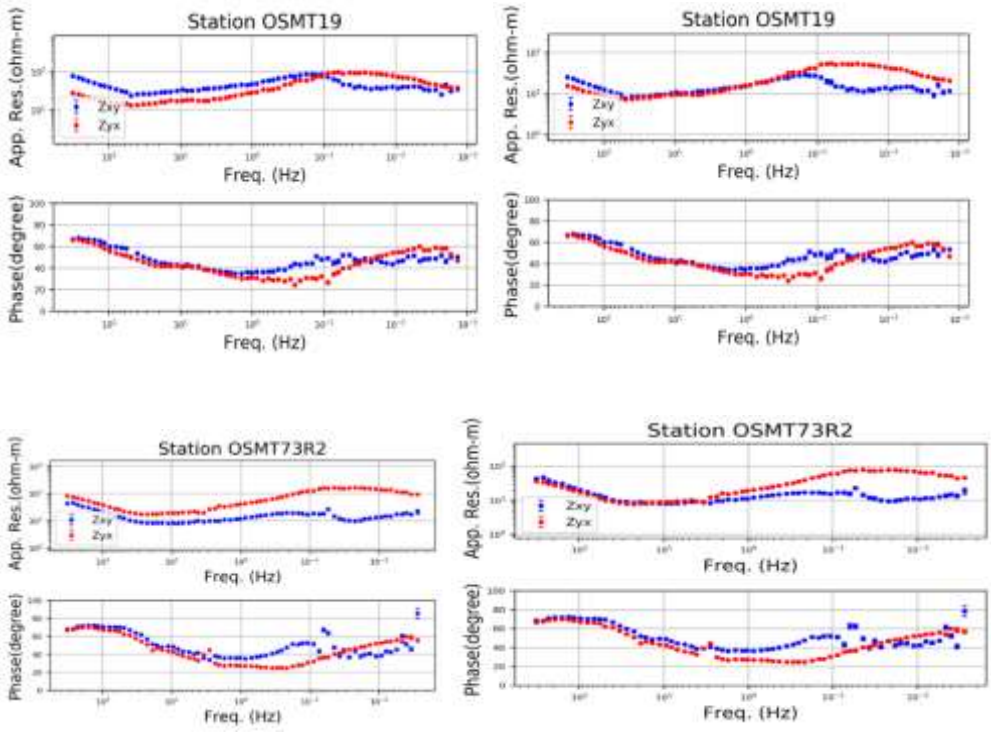

Figure 4.1: Resistivity curves before (left) and after (right) removal of static shifts.

4.2 Data Imaging

MT sounding curves gives results of the expected structures following inversion. Figure 4.2 shows MT sounding curves of TE and TM modes obtained from 23 sites in Olkaria South East geothermal field. The red dots indicate the TE mode and the blue dots indicate TM mode. The apparent resistivity from both modes shows high values at low periods (< 0.01 s) and decreases as the period increases to below 1 s. Subsequently, the apparent resistivity increases up to a period of 10 s before it falls to a period of 100 s.

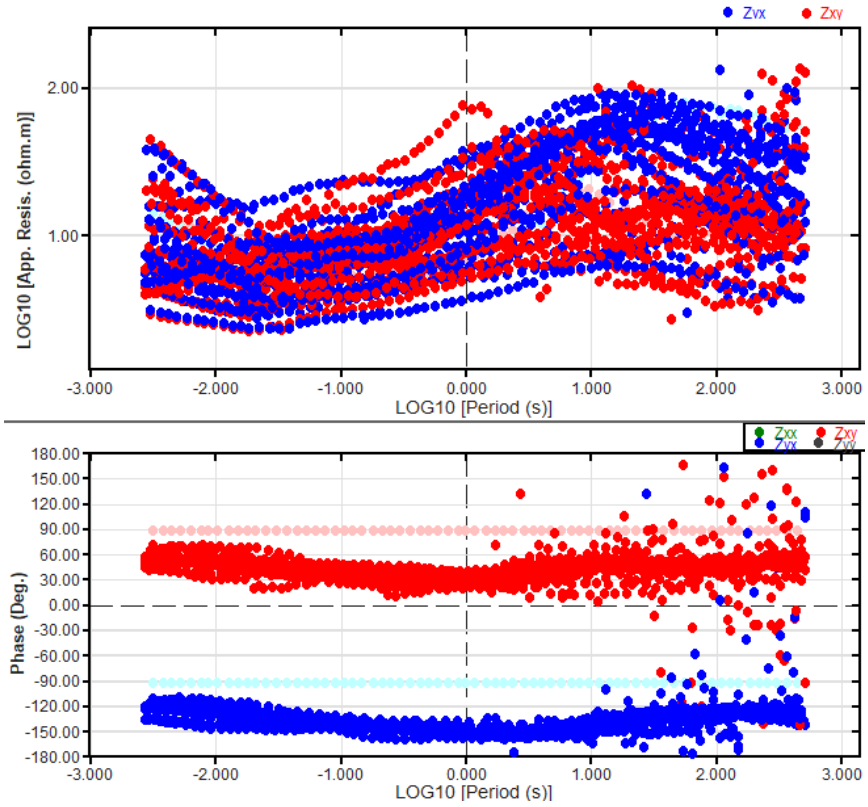

Figure 4.2: Apparent resistivity curves and phase curves from 23 stations in Olkaria south east field respectively.

4.3 Dimensionality Analysis

Dimensionality analysis of MT data is a common procedure for inferring the main properties of the subsurface geo-electric structures such as the strike direction or the

presence of superficial distorting bodies, and helps in determining the most appropriate modeling approach (Martí *et al*., 2010). For this study, swift-skew, bahr-skew, ellipticity and phase tensor methods were used to determine dimensionality of Olkaria South East field.

Swift-Skew

Olkaria South East data, most stations indicate 1D and 2D structures at short periods below 1s given by swift skew values below 0.3 and 3D structures at a period greater than 1s indicated by swift skew values greater than 0.3 as shown in the Figure 4.3 below for soundings OSMT 18R and OSMT 19. One major disadvantage of swift skew is that its affected by noise.

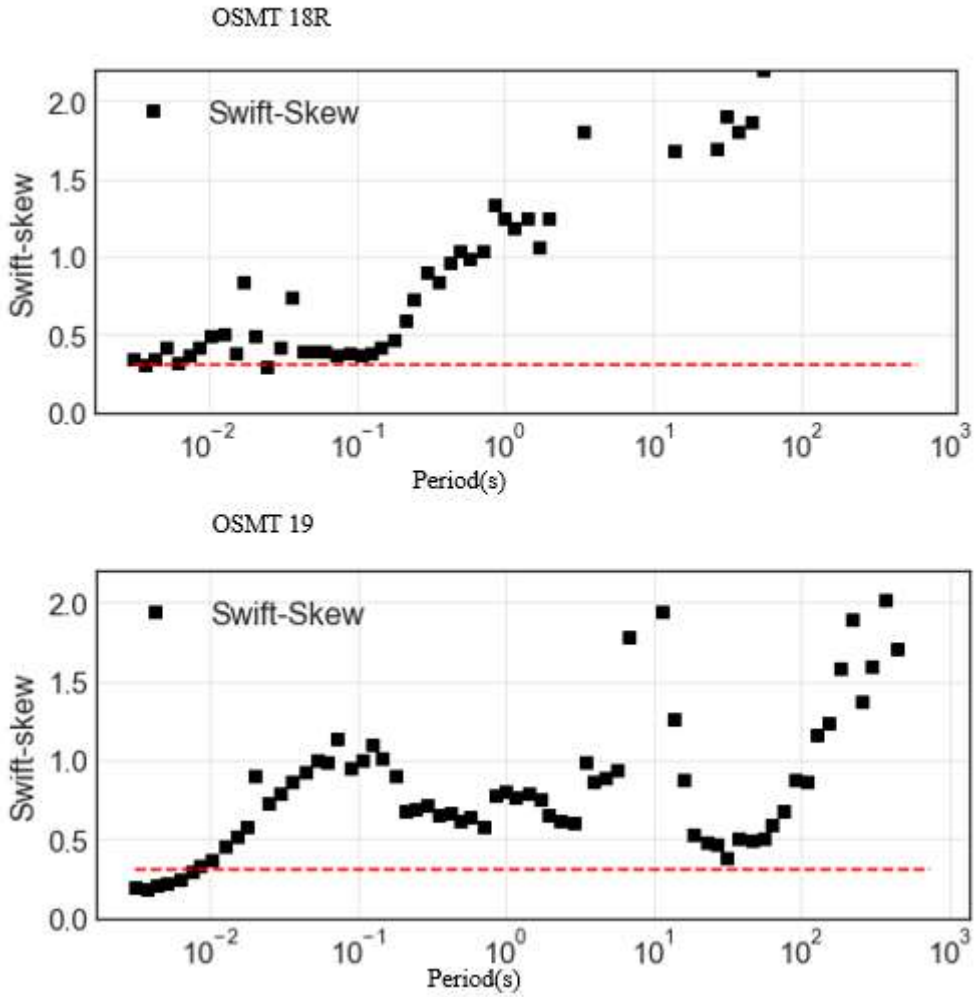

Figure 4.3: Swift skew for stations OSMT 18R and OSMT 19.

Bahr Skew

For Olkaria South East field most stations showed skew values close to zero, below 0.3 at periods less than 0.1 s indicating presence of 1D and 2D structures at shallow depths and skew values greater than 0.3 indicating 3D dimensionality at greater depths as shown by Figure 4.4 below for stations DMT 41 and OSMT 79.

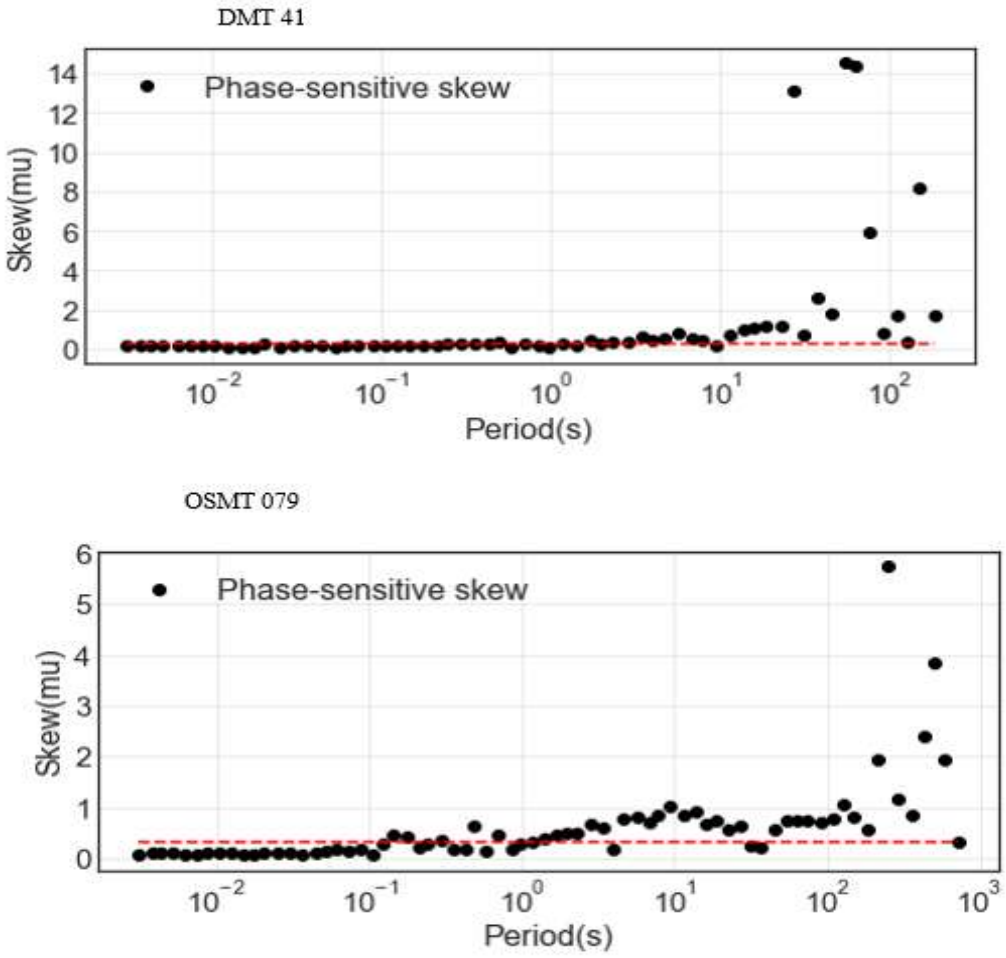

Figure 4.4: Bahr skew for stations DMT 41 and OSMT 079.

Ellipticity

Ellipticity was plotted against period for Olkaria south east MT stations and most of the stations showed low ellipticity values below the 0.1 threshold at short period indicating presence of 1D and 2D structures at shallow depth and high ellipticity values greater than the 0.1 threshold indicating 3D structures at greater depths as shown on the Figure 4.5 for stations DMT 41 and DMT 200. Ellipticity is also sensitive to noise.

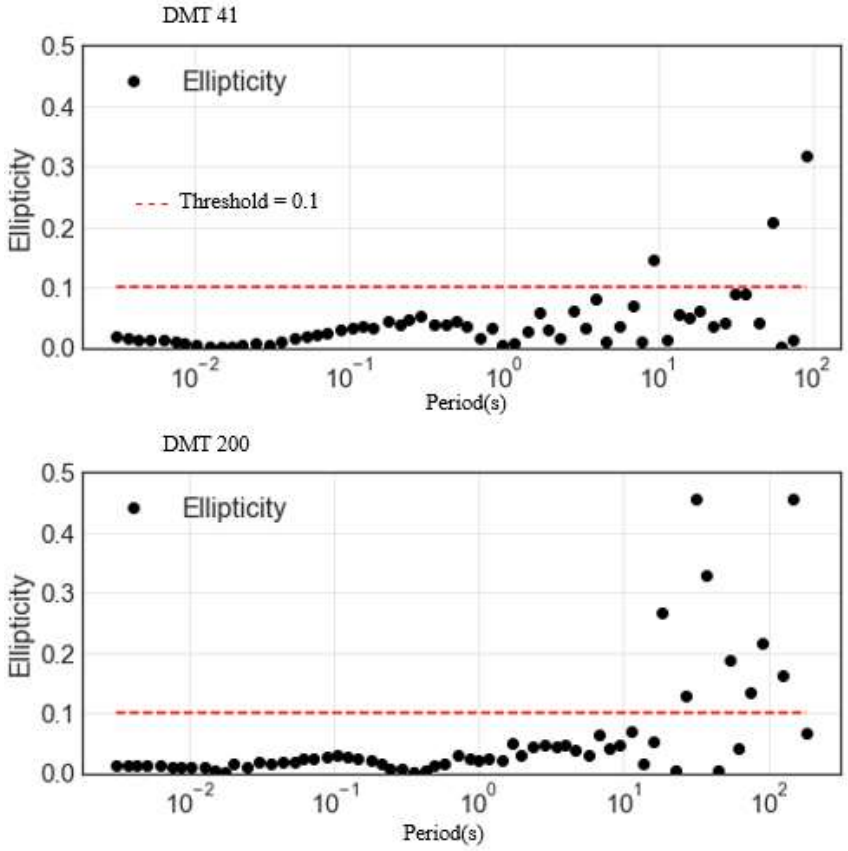

Figure 4.5: Ellipticity for stations DMT 41 and DMT 200.

Phase Tensor

In Olkaria south east, the phase tensor maps plotted at different frequencies reveal the dimensionality of the MT data (Figures 4.6 – 4.9). The dimensionality of the subsurface structures can be inferred from the shapes of the phase tensor and skew angle. At high frequencies above 1Hz (short periods), the phase tensor maps indicate small skew angle ($-3 < \beta < 3$). The shape of the ellipses generally is yellow in color and circular at higher frequencies and elliptical around 1 Hz implying structures at shallow depths are 1-D and 2-D characteristics (Figures 4.6 and 4.7). The phase tensor analysis reveals 3D dimensionality below 1 Hz, characterized by a high skew angle ($\beta < -3$ and $\beta > 3$), red, blue colors and the phase tensors are non-symmetric as indicated in Figure 4.8 and 4.9.

At different depths, the directions of the observed induction arrows are heterogeneous, implying complexity in the distribution of the conductive structures. At longer periods, most vectors are observed to point in one direction, portraying an alignment of conductive structures nearly parallel to the regional geo-electric strike.

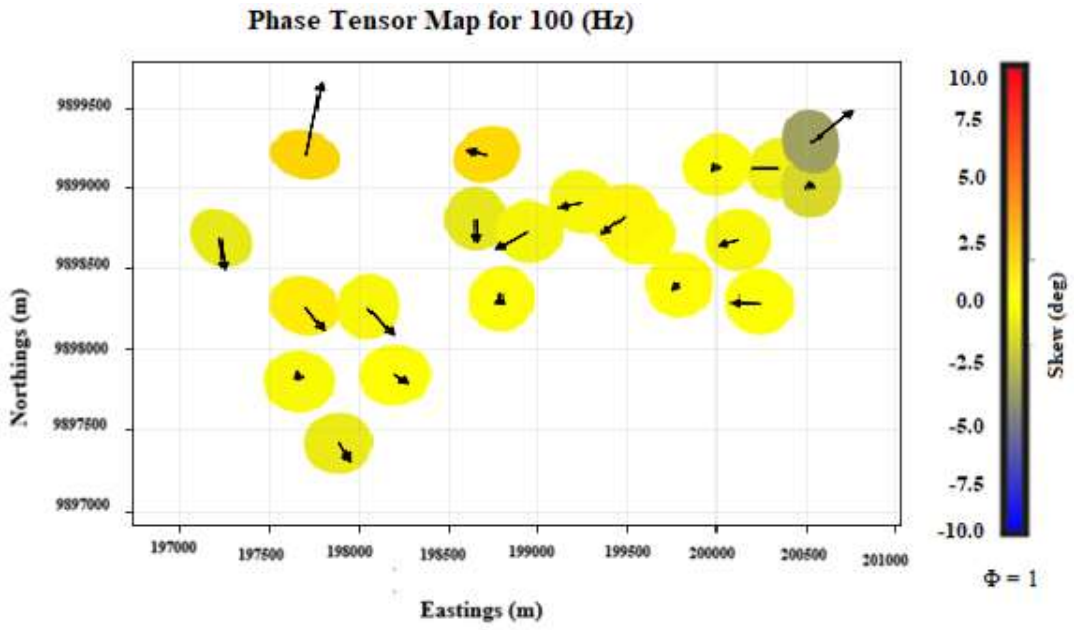

Figure 4.6: The real induction vector, phase tensor ellipses in the Parkinson convention for a frequency of 100Hz.

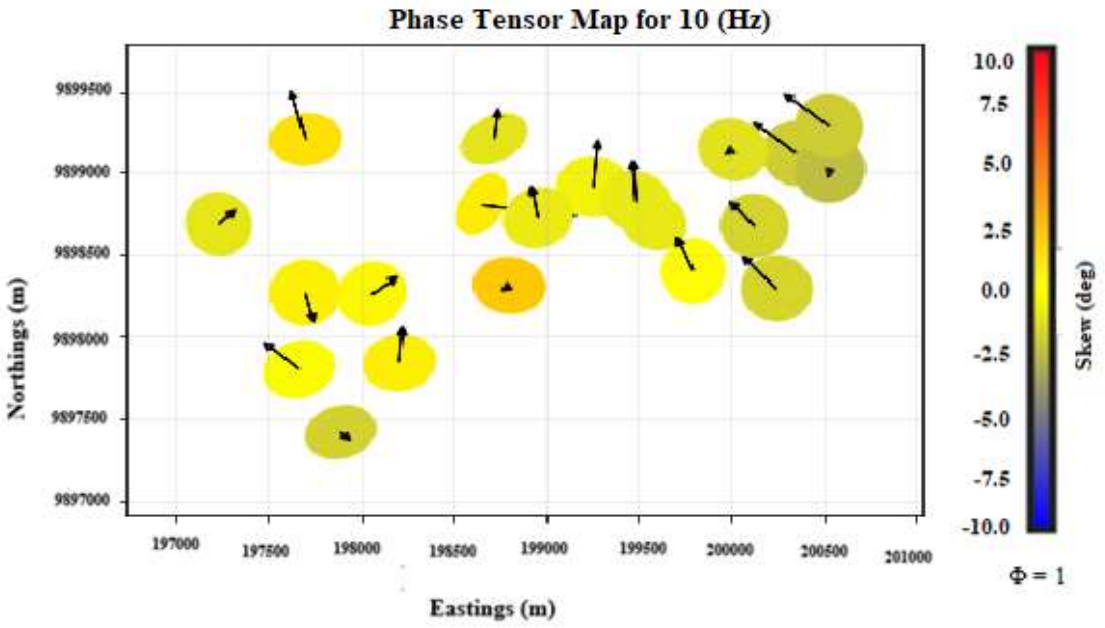

Figure 4.7: The real induction vector, phase tensor ellipses in the Parkinson convention for a frequency of 10Hz.

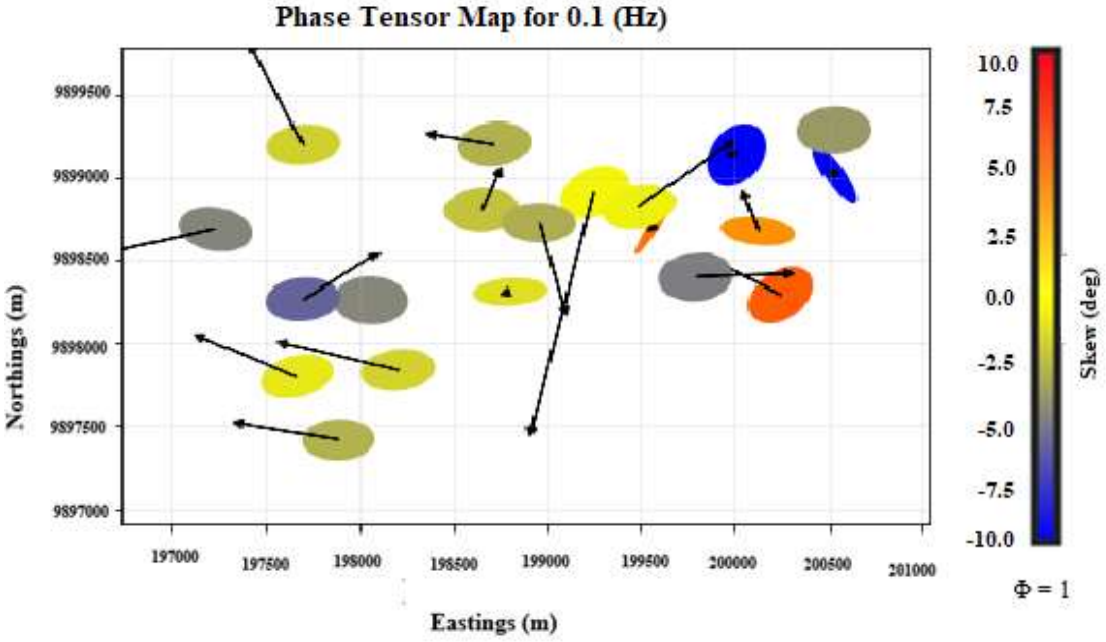

Figure 4.8: The real induction vector, phase tensor ellipses in the Parkinson convention for a frequency of 0.1Hz.

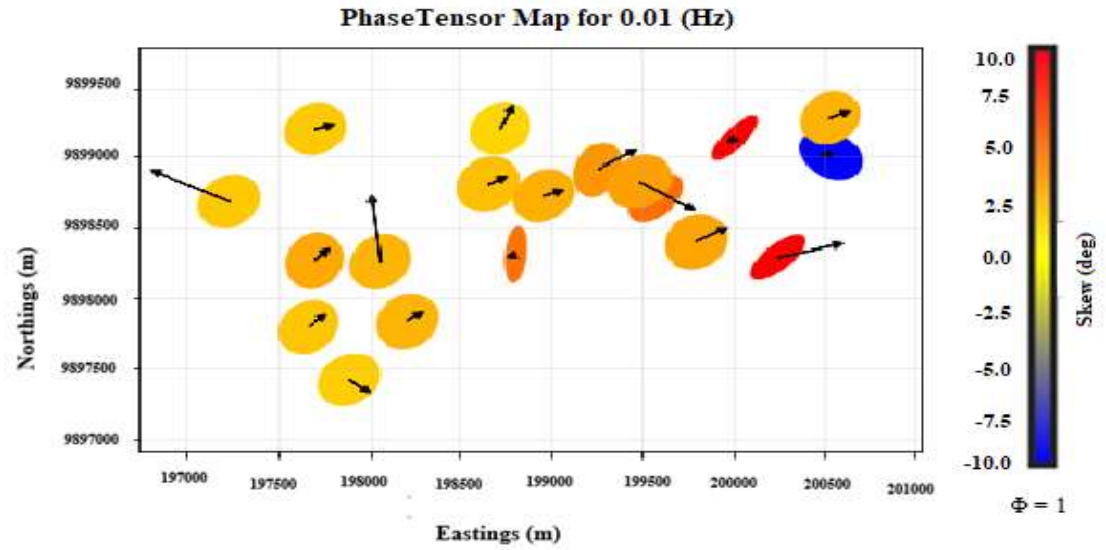

Figure 4.9: The real induction vector, phase tensor ellipses in the Parkinson convention for a frequency of 0.01Hz.

The dimensionality results show 1D and 2D structures at short periods and 3D structures at long periods.

4.4 Strike Estimation

Geoelectric strike must be determined if dimensionality shows there are 2D structures. Figure 4.10 shows a consistent geo-electric strike of N75^{0}W at periods 10^0 – 10^1 s, which conforms to the Olkaria field regional structural trend of NE-SW. The profiles 1 and 2 were constructed nearly perpendicular and parallel to the geo-electric strike direction respectively. Before 2D inversion, the impedance components were rotated N75º W.

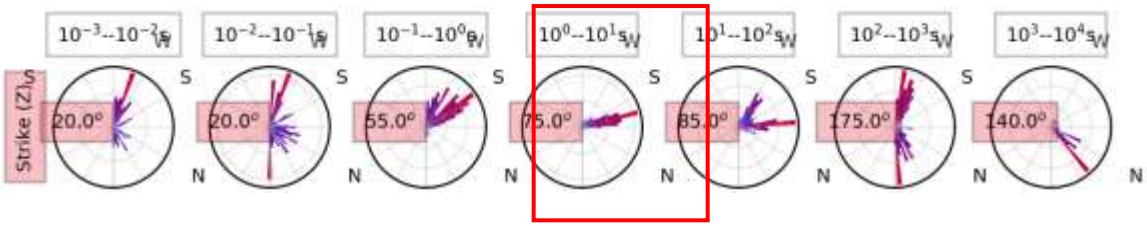

Figure 4.10: The Z strike rose diagram of Olkaria MT data over the period range 10-3 - 103 s.

4.5 MT Data Inversion

4.5.1 1D inversion results

1D models of the Olkaria south east field at each station revealed a high resistivity (~ 100 Ωm) layer at shallow depth with its thickness varying for different stations as shown in Figure 4.11 and 4.12. A second layer with low resistivity is observed with a resistivity ranging between 5-10 Ωm. A third layer with relatively higher resistivity approximately 40 Ωm is observed beneath the conductive layer. The thickness varies for different stations.

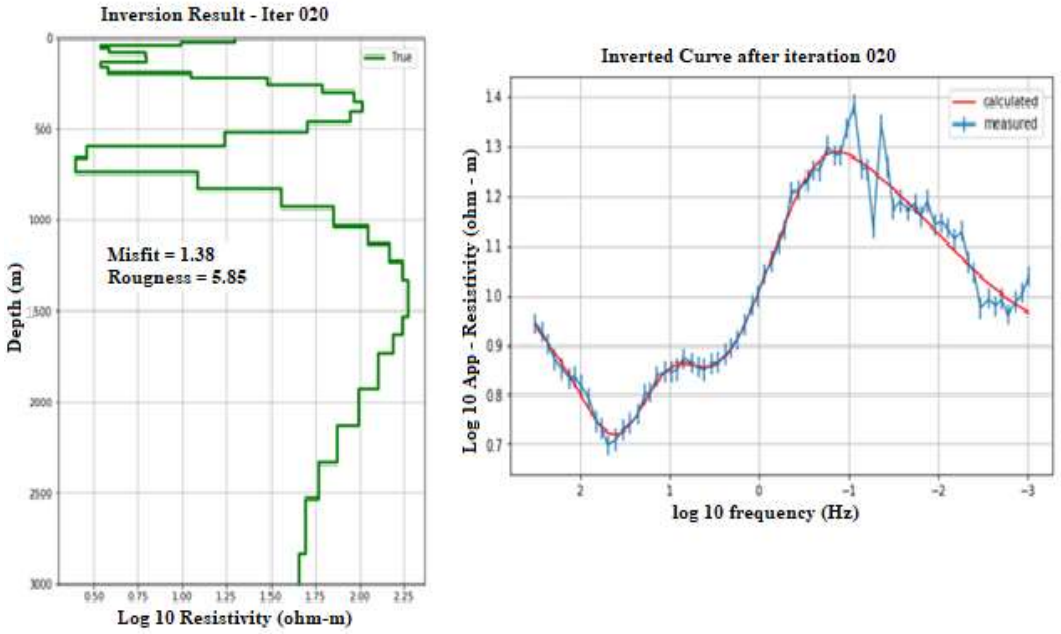

Figure 4.11: 1D model and misfit curve at station OMT 120.

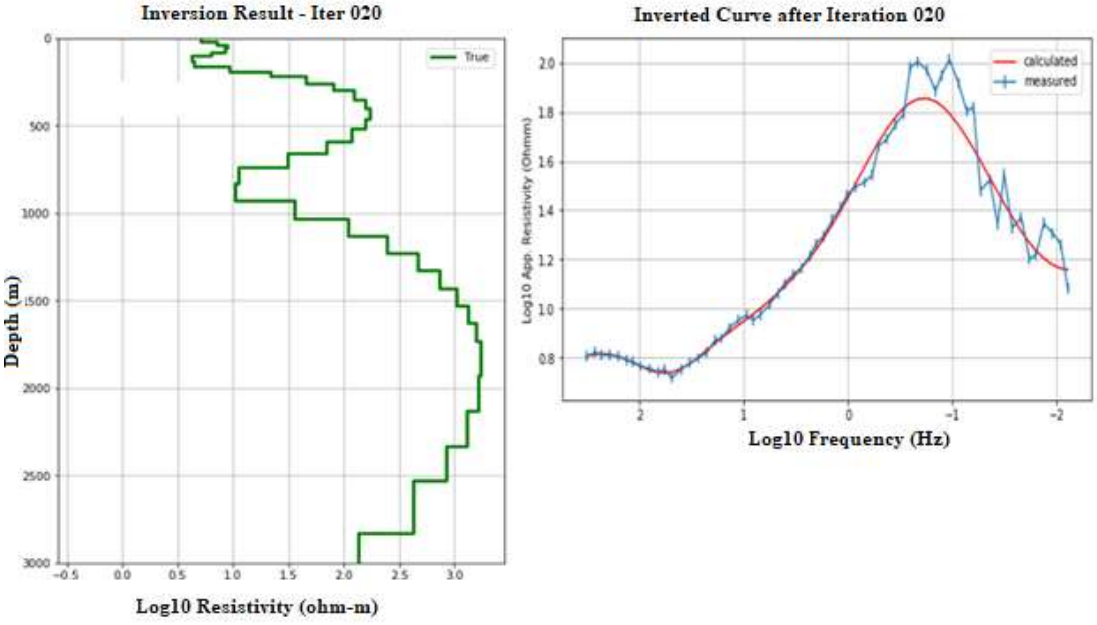

Figure 4.12: 1D model and misfit curve at station DMT 38.

4.5.2 2D inversion results

The models had a minimum root mean square misfit of 1.85 for profile 1 and 1.33 for profile 2.

For profile 2 the pseudo-section plot for TE and TM modes for both observed and predicted responses shows a good fit as shown in Figure 4.13. The TE mode shows a relatively better fit than the TM modes as it shows a small residual. The residual map shows the differences between the observed and predicted responses.

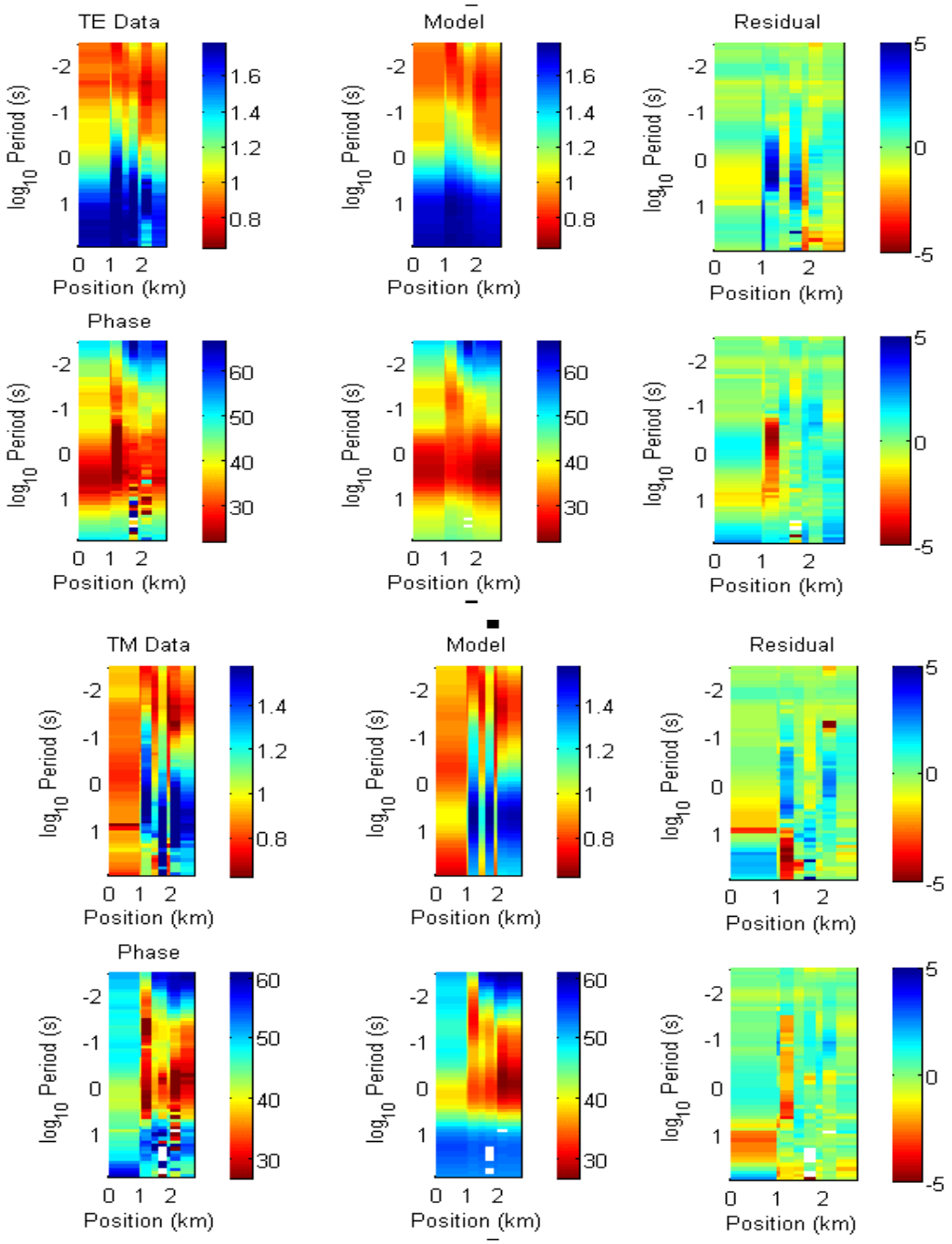

Figure 4.13: Pseudo sections of observed and calculated apparent resistivity and phase for TE and TM mode for Profile 2.

The resistivity models obtained from two profiles are as shown on Figure 4.14 and 4.15. The results revealed conductive bodies C1 –C3 and resistive anomalies R1-R3. Figure 4.14 shows a conductive body C1 (< 10 Ω*m*) located at a depth of about 0.5 -3 km and a resistive body R1 (> 100 Ω*m*) at a depth of 3-5km. Figure 4.15 shows resistive bodies R2 and R3 separated by a conductive structure C2 running from NE to SW. C3 is located at approximately 2-2.5 km on the east side and separated from C2 by R3. It is also overlain by a conductive layer of approximately 0.5 km and running deeper on the east side.

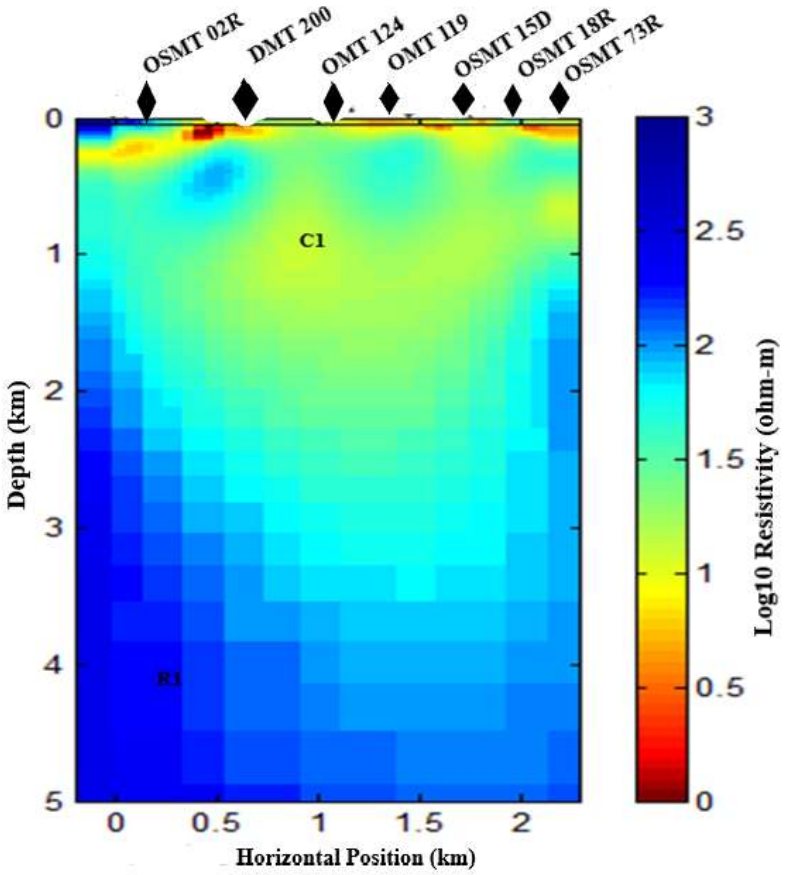

Figure 4.14: 2D resistivity cross-section model profile 1.

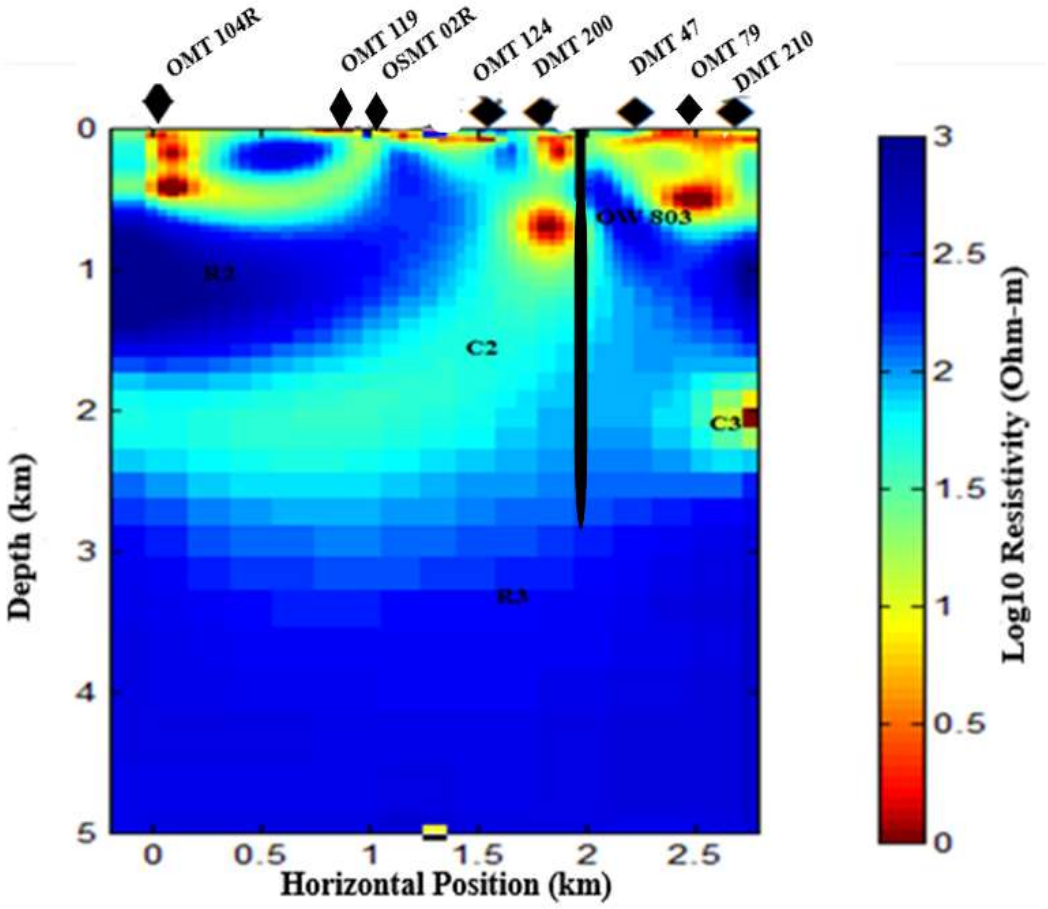

Figure 4.15: 2D resistivity cross-section model profile 2.

4.5.1 3D Inversion results

The data misfit of the final model is satisfactory with limited over and under fitted sections as shown in figure 4.16 and 4.17.

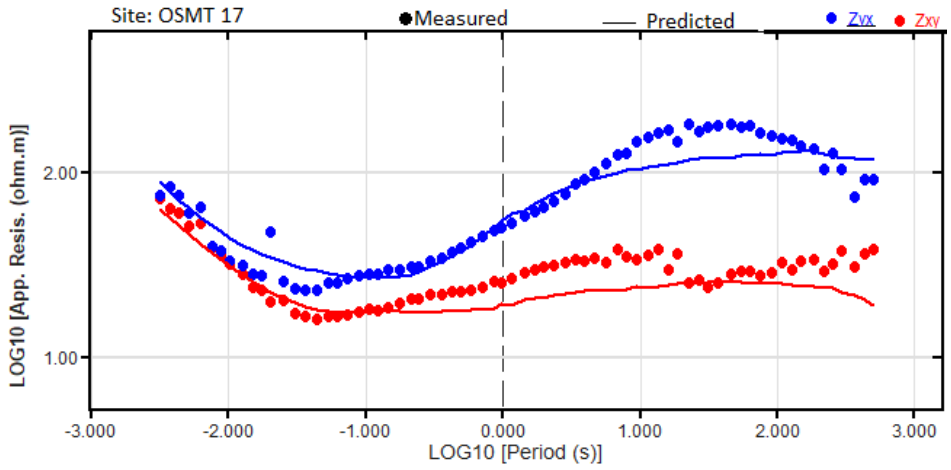

Figure 4.16: Data misfit between the observed and calculated apparent resistivity of Zxy (red dots) and Zyx (blue dots) components for station OSMT17.

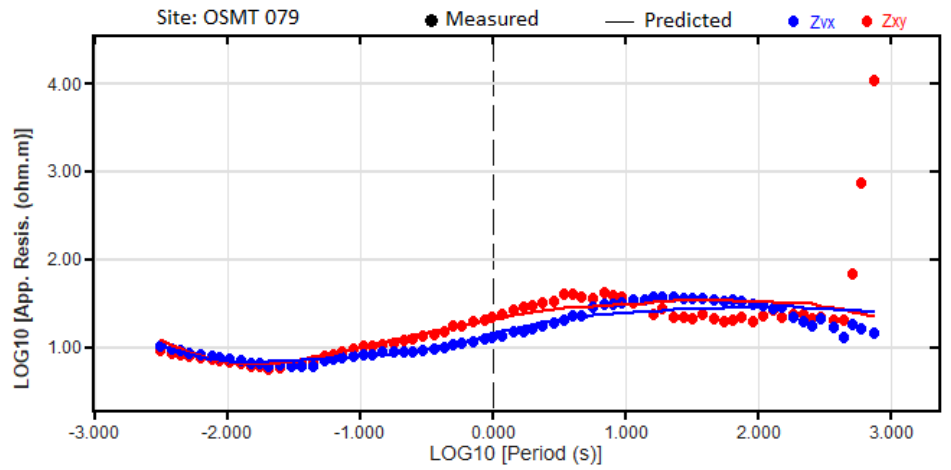

Figure 4.17: Data misfit between the observed and calculated apparent resistivity of Zxy (red dots) and Zyx (blue dots) components for station OSMT 79.

The 3D model for the Olkaria South East field (Figure 4.18) has three distinctive layers with the first layer having a resistivity > 80 Ωm extending to about 200 m underlain by a low conductivity layer of < 10 Ωm with a thickness of approximately 0.5- 1 km and beneath it is a relatively high resistivity to high resistive layer > 100 Ωm at a depth of approximately 2 km extending down to 10 km.

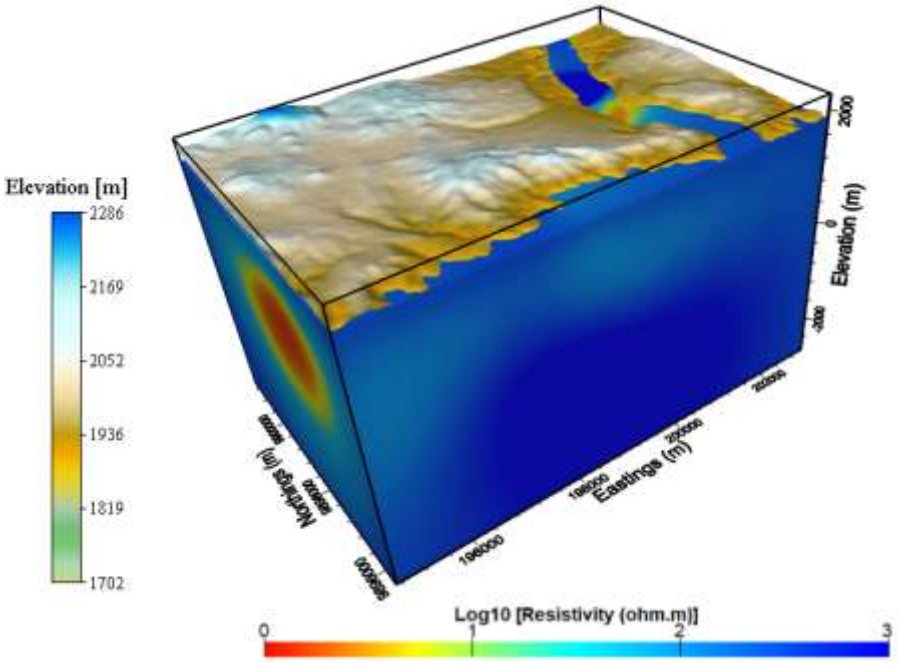

Figure 4.18: 3D model of Olkaria South East.

The 3D resistivity models for profile 1 and 2 (Figure 4.19 and 4.20) shows conductive layers C1 and C2 (5- 10 Ωm) and resistive layers R1, R2 and R3. Both profiles show a highly resistive layer especially on the central part with a thickness of around 500 m and a resistivity of > 100 Ωm. Below it, conductive layer C1 and C2 extends to about 1km depth for both profiles. Beneath it is a highly resistive layer R2 and R3 with a resistivity > 100 Ωm at approximately 2.5 km all the way to 5 km.

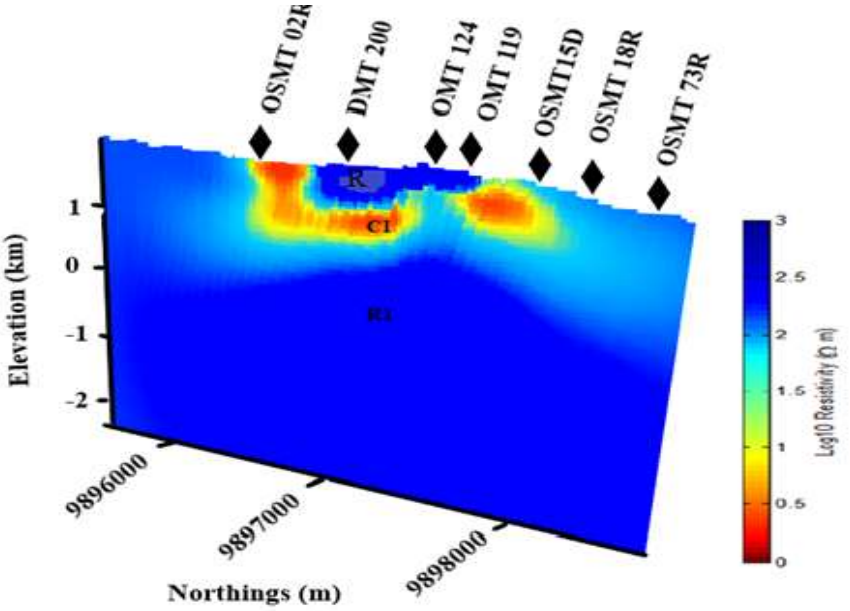

Figure 4.19: 3D resistivity model for profile 1.

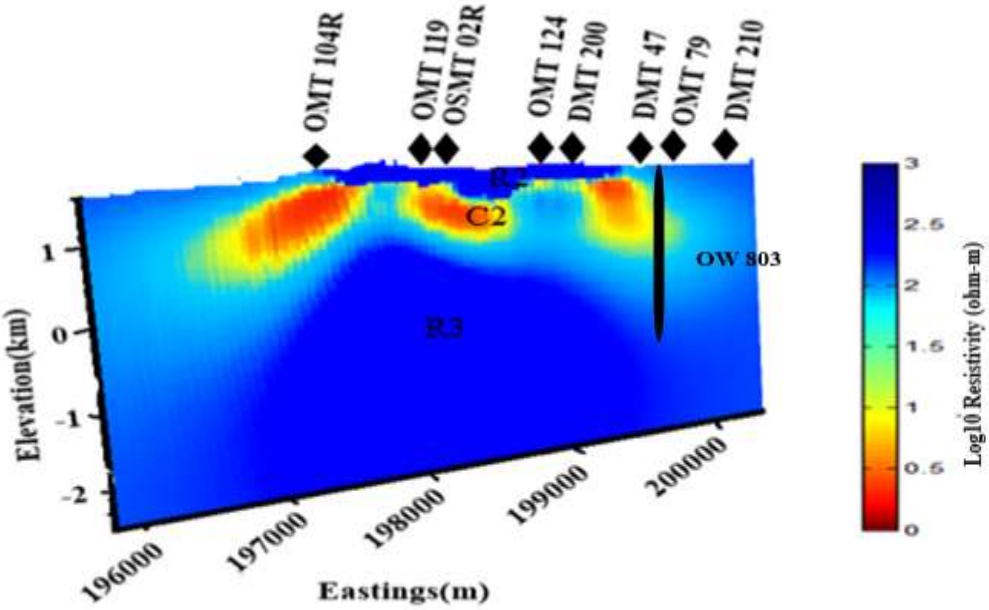

Figure 4.20: 3D resistivity model for profile 2.

The iso surface model Figure 4.21 below, shows the variation of resistivity and the location of the drilled wells in the area. It shows a conductive structure of up to a depth of 500m and a resistive zone below it.

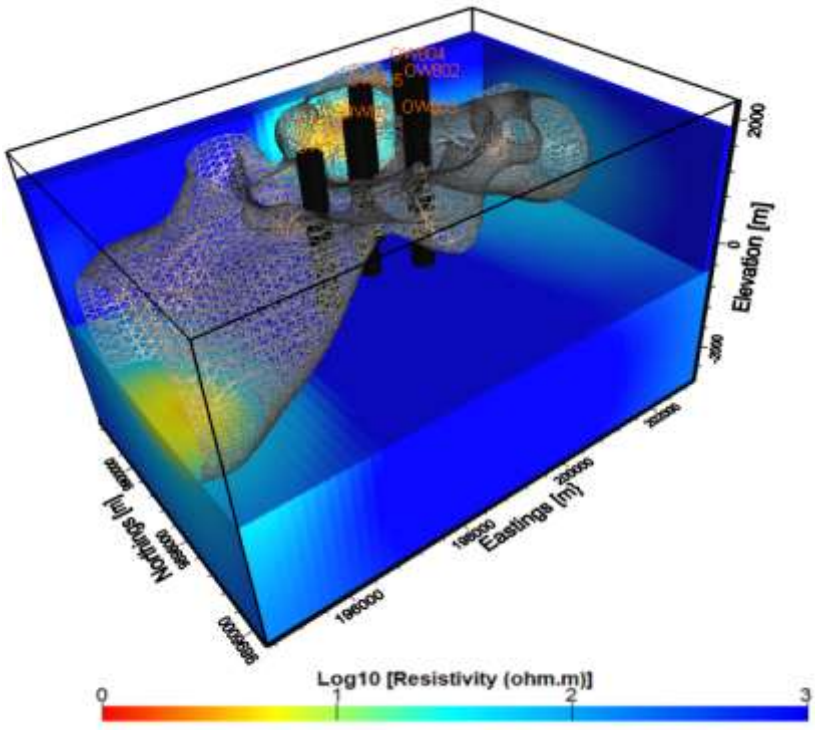

Figure 4.21: Iso- surface model of Olkaria south east

4.5.3 2D Inversion Versus 3D Inversion

The 2D and 3D inversion models (Figure 4.22) show similar structures at shallow depths with both models showing a conductive zone < 10 Ωm beneath a highly resistive zone. However, at depth, the 3D model gives a better resolution with a highly resistive layer at a depth of 2 to 3km with a resistivity of > 100 Ωm which is different from the resistivity mapped by the 2D inversion of 40-60 Ωm. The 2D results at depth shows a characteristic of a geothermal reservoir resistivity of between 10 - 40 Ωm which is not present in the 3D.

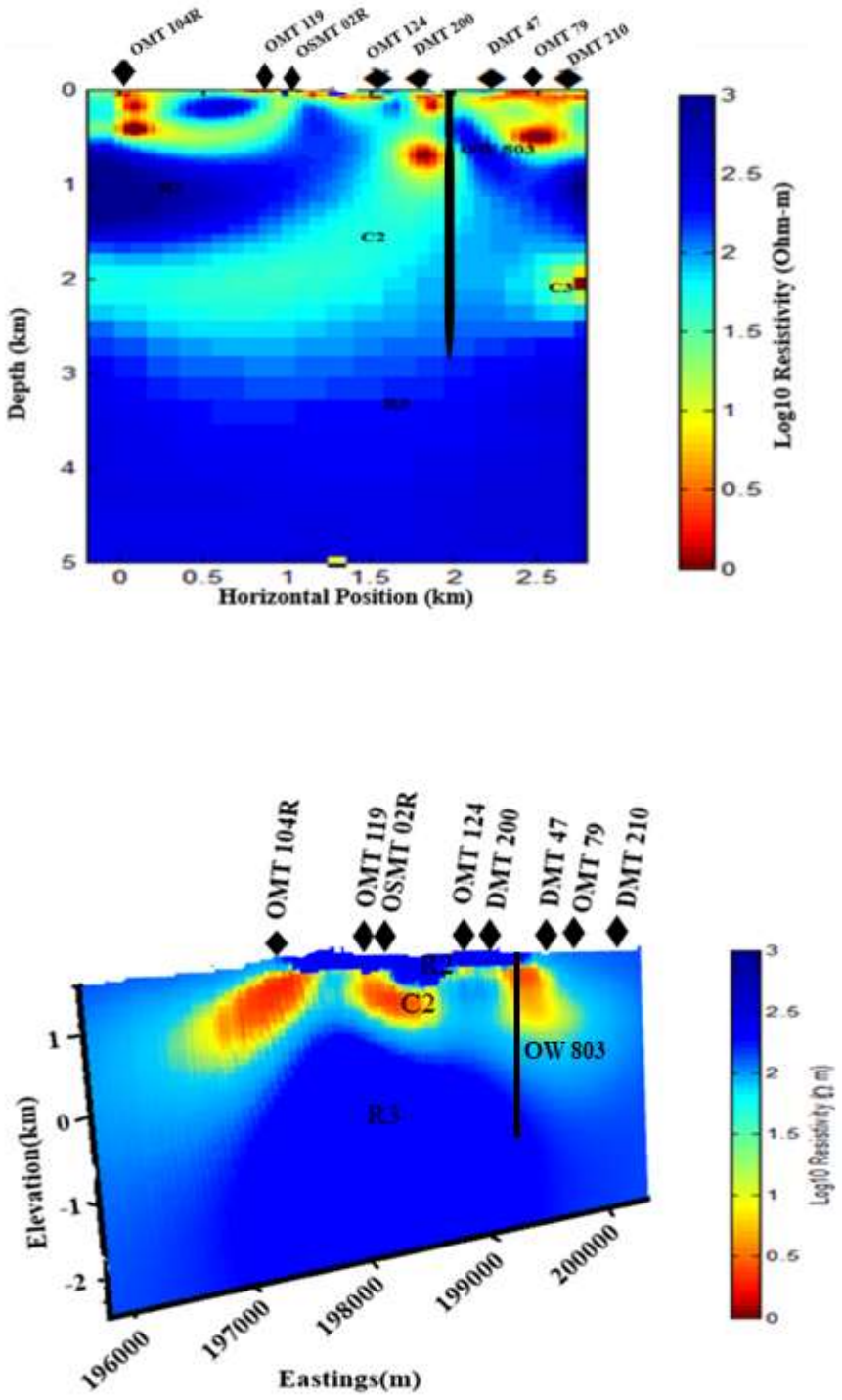

Figure 4.22: 2D and 3D models for profile 2 respectively.

4.6 Temperature Profiles

The temperature profiles below (Figures 4.23 and 4.24) taken over a period of time show temperature increases with depth. At a depth of 2600m, where the intrusion is intercepted, the injection profiles show a sharp kick and the temperature rises. However, after sometime the temperatures reverse and does not exhibit sharp kicks.

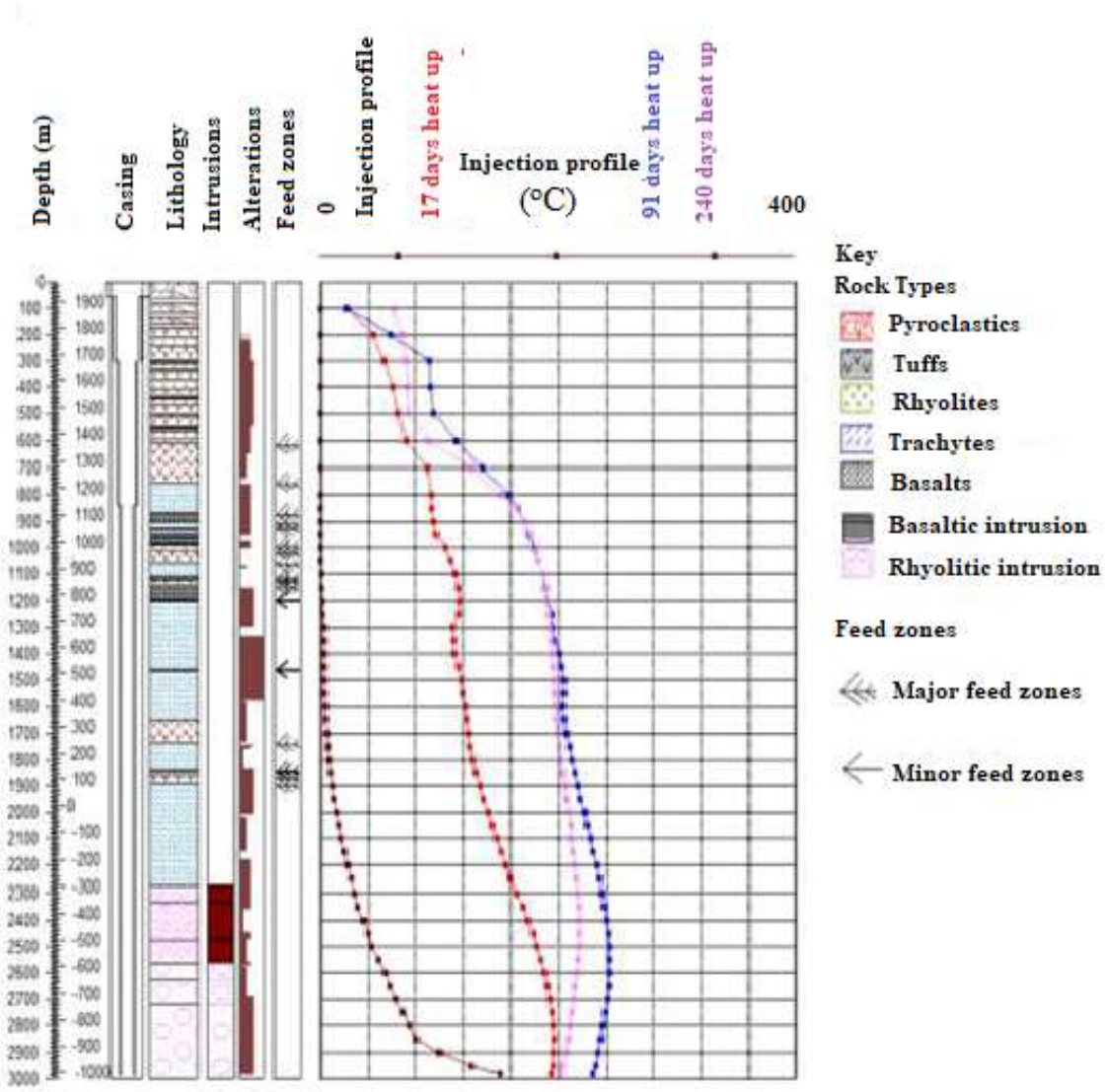

Figure 4.23: Temperature profile for well 803.

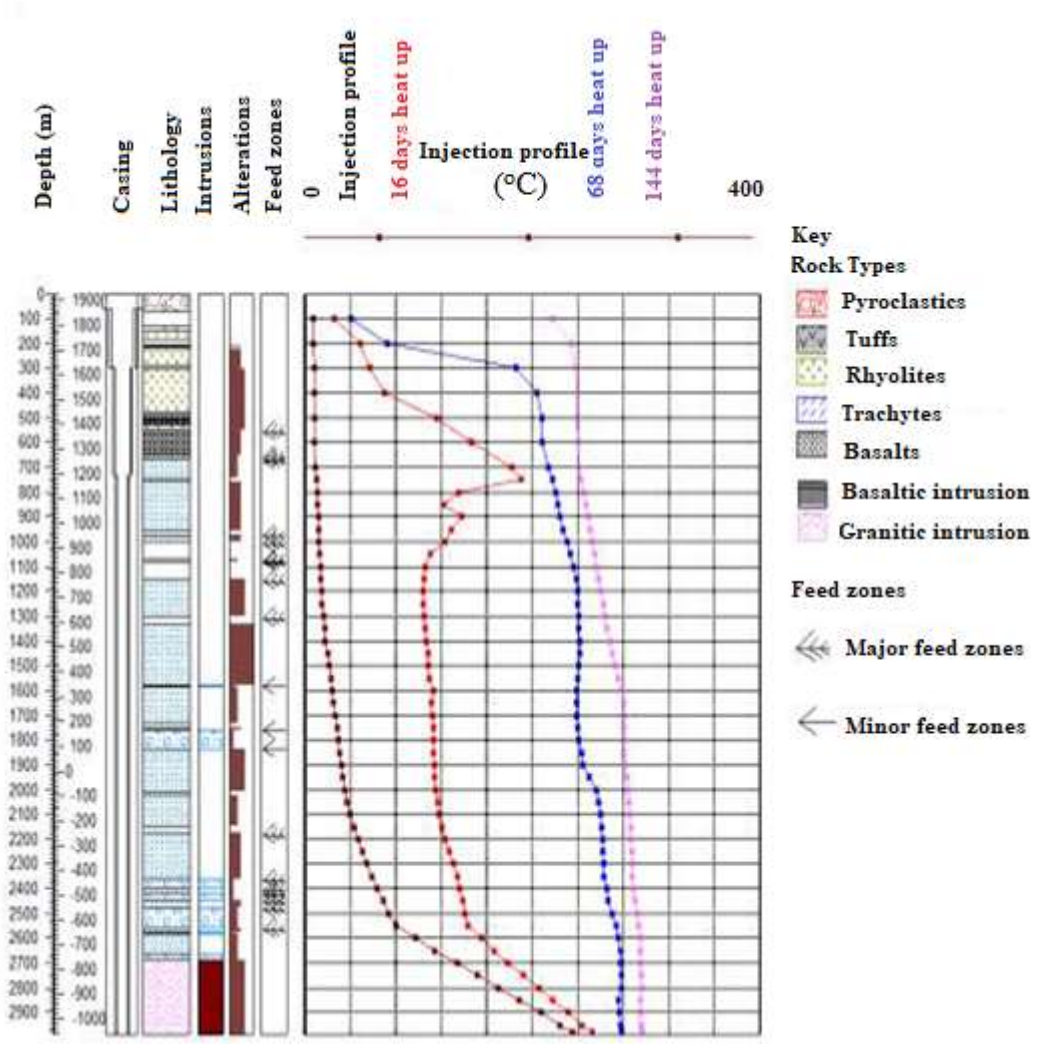

Figure 4.24: Temperature profiles for well 802.

4.7 Conceptual Model

The updated conceptual model of Olkaria South East as shown in figure 5.1 was constructed from the 3D models results. It shows characteristics of a high enthalpy geothermal system with a high resistive unaltered layer, low resistive caprock (<10 Ωm), recharge areas and a reservoir. However, the reservoir does not meet the requirements of a high enthalpy geothermal reservoir which is characterized by high temperatures and a relatively high resistivities of (10-60 Ωm). The geothermal reservoir in Olkaria South East field from the resistivity models has a resistivity of > 100 Ωm and temperatures of < 250^{o}C as shown on the temperature logs.

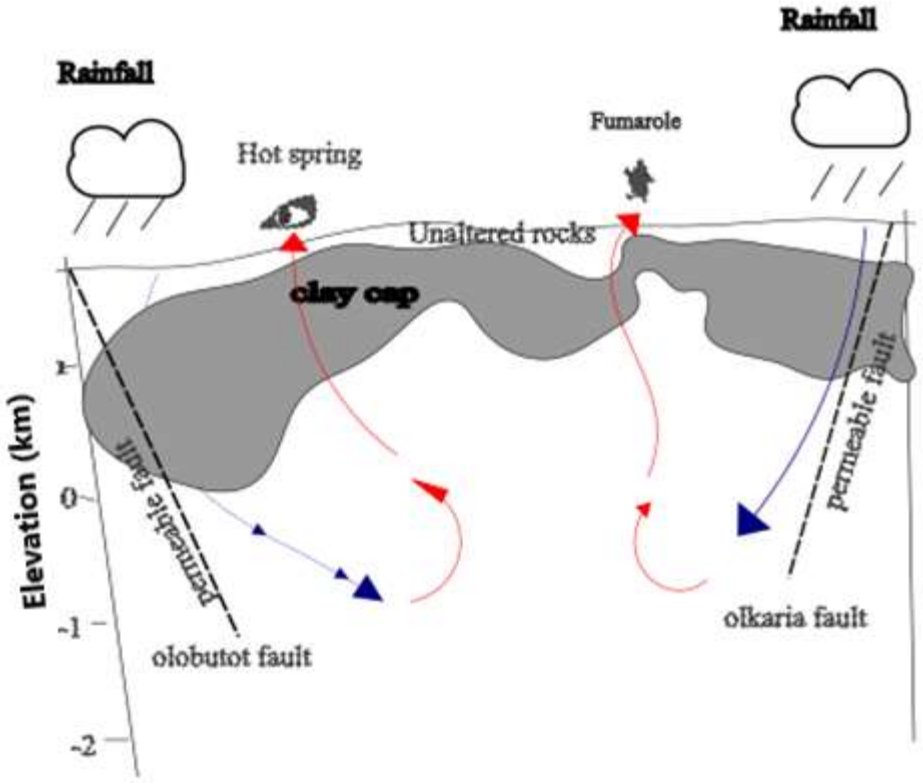

Figure 4.25: Conceptual model of Olkaria South East field.

CHAPTER FIVE

CONCLUSIONS AND RECOMMENDATIONS

5.1 Conclusion

The resistivity of the Olkaria South East field is revealed from the MT data inversion. The 1-D models at each station revealed a high resistivity layer (> 80 Ωm) at shallow depths, and its thickness varies from station to station. A second conductive layer (< 10 Ωm) is recognized at different depths in all the stations. The third layer with higher resistivities (> 100 Ωm) is observed at most stations beneath the conductive layer. Most of the geological structures in Olkaria South East geothermal field trend in the North to South direction, and they are likely to control the movement of fluid in the geothermal field. From the 2D and 3D resistivity models three layers have been revealed. The first layer has a high resistivity (~80 Ωm) which could be interpreted as the unaltered volcanic rock formation possibly from the pyroclastic cover. The second layer has a low resistivity (5-10 Ωm) interpreted as the cap rock. The low resistivities are attributed to alteration minerals such as smectites and illites. The third layer has a relatively high resistivity (> 80 Ωm) and is interpreted as the geothermal reservoir. The high resistivities could be attributed to the cold inflow in the region which is traversed by the major Olobutot fault which is the major fault that feeds Olkaria region hence the temperatures reversals and low pressures at depth. The 3D method proved to be a powerful modelling technique in delineating the subsurface structure and hence, I was able to achieve all the objectives.

5.2 Recommendations

From the above findings, the area has an extensive geothermal reservoir and while it is not ideal for citing a production well, it can be used as a reinjection zone. Nevertheless, the findings were done on a small survey area due to time constraints. These findings could be concluded by using a large MT dataset covering a bigger area, or by use of any other detailed geophysical survey such as gravity and seismics.

REFERENCES

Abdelfettah, Y., Tiercelin, J. J., Tarits, P., Hautot, S., Maia, M., & Thuo, P. (2016). Subsurface structure and stratigraphy of the northwest end of the Turkana Basin, Northern Kenya Rift, as revealed by magnetotellurics and gravity joint inversion. *Journal of African Earth Sciences*, *119*, 120-138.

Ballzus, C., Frimannson, H., Gunnarsson, G. I., & Hrolfsson, I. (2000). The geothermal power plant at Nesjavellir, ICELAND. In *Proc. World Geothermal Congress* (pp. 3109–3114). Kyushu-Tohoku, Japan

Berdichevsky, M. N., Dmitriev, V. I., & Pozdnjakova, E. E. (1998). On two-dimensional interpretation of magnetotelluric soundings. *Geophysical Journal International*, *133*(3), 585-606.

Berdichevsky, M. N., & Dmitriev, V. I. (2002). *Magnetotellurics in the context of the theory of ill-posed problems*. Society of Exploration Geophysicists.

Berdichevsky, M. N., & Dmitriev, V. I. (2008). *Models and methods of magnetotellurics*. Springer Science & Business Media.

Caldwell, T. G., Bibby, H. M., & Brown, C. (2004). The magnetotelluric phase tensor. *Geophysical Journal International*, *158*(2), 457-469.

Cagniard, L. (1953). Basic theory of the magneto-telluric method of geophysical prospecting. *Geophysics*, *18*(3), 605-635.

Clarke, M. C. G., Woodhall, D. G., Allen, D., & Darling, G. (1990). Geology, volcanological and hydrogeological controls on the occurrence of geothermal activity in the area surrounding Lake Naivasha, Kenya. *Report of the Ministry of Energy of Kenya*.

Constable, S. C., Parker, R. L., & Constable, C. G. (1987). Occam's inversion: A practical algorithm for generating smooth models from electromagnetic sounding data. *Geophysics*, *52*(3), 289-300.

Cumming, W., & Mackie, R. (2007). 3D MT resistivity imaging for geothermal resource assessment and environmental mitigation at the glass mountain KGRA, California. *GRC Transactions*, *31*, 331-334.

deGroot-Hedlin, C., & Constable, S. (1990). Occam's inversion to generate smooth, two-dimensional models from magnetotelluric data. *Geophysics*, *55*(12), 1613-1624.

Dickson, M. H., & Fanelli, M. (2005). Geothermal energy: utilization and technology,. Earthscan, an imprint of James & James.

Egbert, G. D., & Kelbert, A. (2012). Computational recipes for electromagnetic inverse problems. *Geophysical Journal International*, *189*(1), 251-267.

Filbandi Kashkouli, M., Kamkar Rouhani, A., Morad zadeh, A., & Assi, H. (2016). Dimensionality analysis of subsurface structures in magnetotellurics using different methods (a case study: oil field in Southwest of Iran). *Journal of Mining and Environment*, *7*(1), 119-126.

GDC. (2018). *Steam status and resource assessment of Menengai geothermal project, Kenya. Internal report*.

Griffiths, D. J. (1999). *Introduction to Electrodynamics* (3 rd Editi). Prentice Hall, New Jersey.

Hersir, G. P., & Árnason, K. (2009). Resistivity Methods–MT. *SDG Short Course I on Exploration and Development of Geothermal Resources, organized by UNU-GTP, GDC and KenGen, at Lake Bogoria and Lake Naivasha, Kenya*, 10-31.

Hochstein, M. P., Zhongke, Y., & Ehara, S. (1990). The Fuzhou geothermal system (People's Republic of China): modelling study of a low temperature fracture-zone system. *Geothermics*, *19*(1), 43-60.

Johnston, J. M., Pellerin, L., & Hohmann, G. W. (1992). Evaluation of electromagnetic methods for geothermal reservoir detection. *Transactions- Geothermal Resources Council*.

Kanda, I. K., Rankas, L., Bett, E. K., Kipngok, J. K., Mutonga, M., Sosi, B., ... & Mwawasi, H. (2011). *Paka Prospect: Investigations of its geothermal potential* (Vol. 10, p. 14pp). GDC Internal report.

Kelbert, A., Meqbel, N., Egbert, G. D., & Tandon, K. (2014). ModEM: A modular system for inversion of electromagnetic geophysical data. *Computers & Geosciences*, *66*, 40-53.

Keller, G. V. (1983). *Frequency and transient soundings*. Elsevier.

Key, K. (2011). OCCAM1DCSEM: An Open-Source Inversion Program for Generating Smooth 1D Models from Controlled-Source Electromagnetic and Magnetotelluric Data. OCCAM1DCSEM instruction manual, Scripps Institution of Oceanography University of California, San Diego.

KPLC. (2018). Annual report and financial statements for the year ended 30th June 2018. Retrieved from https://www.kplc.co.ke/AR2018/KPLC Annual Report 17_12_2018_Wed.pdf

Lagat, J. K., Omenda, P. O., Mungania, J., Mariita, N. O., Wambugu, J. M, Opondo, K. Ofwona, C., Mwawongo, G., Kubo, B. M., & Wetangula, G. (2007). Geo-scientific Evaluation of the Paka Geothermal Prospect, *KenGen Internal report*, 60,7pp.

Lichoro, C.M., (2010). Joint 1-D inversion of TEM and MT data from Olkaria domes geothermal area. Kenya. Trans. - Geotherm. Resour. Counc. 34 (2), 802–808.

Martí, A., Queralt, P., Ledo, J., & Farquharson, C. (2010). Dimensionality imprint of electrical anisotropy in magnetotelluric responses. *Physics of the Earth and Planetary Interiors*, *182*(3-4), 139-151.

Martí, A. (2006). *Magnetotelluric Investigation of Geoelectrical Dimensionality and Study of the Central Betic Crustal Structure, A*.

Maxwell, J. C. (1865). VIII. A dynamical theory of the electromagnetic field. *Philosophical Transactions of the Royal Society of London*, *155*, 459–512.

Meqbel, N. M. M. (2009). *The electrical conductivity structure of the Dead Sea Basin derived from 2D and 3D inversion of magnetotelluric data* (Doctoral dissertation).

Mulwa, J., & Mariita, N. (2013). A comparative analysis of gravity and microseismic results from Arus-Bogoria geothermal prospect, Kenya. *Scholarly Journal of Scientific Research and\Essay (SJSRE), ISSN*, 2315-6163.

Mulwa, J. K., and Mariita, N. O. (2015). Dyking processes in Arus-Bogoria geothermal prospect in Kenya revealed using gravity and microseismic data. In *37th New Zealand Geothermal Workshop: The next 10,000 Megawatts*. University of Auckland, New Zealand Geothermal Association, 37, 20-23.

Munyiri, S. K. (2016). *Structural mapping of Olkaria Domes geothermal field using geochemical soil gas surveys, remote sensing and GIS* (Doctoral dissertation).

Mwangi, A. W., Mickus, K., & Serpa, L. (2018). Dimensionality Analysis of the Olkaria Geothermal Field, East Africa Rift.

Naidu, G. D. (2012). Magnetotellurics: Basic theoretical concepts. In *Deep Crustal Structure of the Son-Narmada-Tapti Lineament, Central India* (pp. 13-35). Springer, Berlin, Heidelberg.

Ofwona, C. (2008). Geothermal resource assessment–Case example, Olkaria I. *Short Course III on Exploration for Geothermal Resources, UNU-GTP*, *3*, 18-19.

Ofwona, C. O. (2002). *A reservoir study of Olkaria East geothermal system, Kenya*. United Nations University, Geothermal Training Programme.

Omenda, P., & Simiyu, S. (2015). Country update report for Kenya 2010-2014. In *Proceedings World Geothermal Congress* (pp. 19-25).

Omenda, P. A. (2000). Anatectic origin for comendite in Olkaria geothermal field, Kenya rift: geochemical evidence for syenitic protolith. *African Journal of Science and Technology*, 1(2), 39-47.

Onacha, S.A., Mungania, J., (1993). Surface exploration of Domes Area: An extension of Olkaria Geothermal field. In: Proceedings 15th NZ Geothermal Workshop, pp. 93–98.

Ouma, P.A (2010). Geothermal exploration and development of the Olkaria geothermal field. *Proceedings if Short Courses V on Exploration for Geothermal Resources*

Palacky, G. (1988). Resistivity characteristics of geologic targets. In *Electromagnetic methods in applied geophysics, 1* (pp. 53–129).

Parasnis, D. S. (1997). Principles of Applied Geophysics: Chapman and Hall. *London, England*, 124-125.

Parker, E. N. (1958). Dynamics of the interplanetary gas and magnetic fields. *The Astrophysical Journal*, *128*, 664.

Pranata, E., Irawati, S. M., & Niasari, S. W. (2017). Magnetotelluric Data Analysis using Swift Skew, Bahr Skew, Polar Diagram, and Phase Tensor: a Case Study in Yellowstone, US: Magnetotelluric Data Analysis using Swift Skew, Bahr Skew,

Polar Diagram, and Phase Tensor. *Proceedings of the Pakistan Academy of Sciences: A. Physical and Computational Sciences*, *54*(3), 311-317.

Ranganayaki, R. P. (1984). An interpretive analysis of magnetotelluric data. *Geophysics*, *49*(10), 1730-1748.

Rodi, W., & Mackie, R. L. (2001). Nonlinear conjugate gradients algorithm for 2-D magnetotelluric inversion. *Geophysics*, *66*(1), 174-187.

Simiyu, S. M. (2010). Status of geothermal exploration in Kenya and future plans for its development. In *Proceedings world geothermal congress* (pp. 25-29).

Simpson, F., & Bahr, K. (2005). *Practical magnetotellurics*. Cambridge University Press.

Siripunvaraporn, W., Uyeshima, M., & Egbert, G. (2004). Three-dimensional inversion for Network-Magnetotelluric data. *Earth, planets and space*, *56*(9), 893-902.

Siripunvaraporn, W., & Egbert, G. (2000). An efficient data-subspace inversion method for 2-D magnetotelluric data. *Geophysics*, *65*(3), 791-803.

Swesco-Virkir. (1976). *Feasibility report for the Olkaria geothermal project.* United Nations, Government of Kenya, report.

Telford, W. M., Telford, W. M., Geldart, L. P., & Sheriff, R. E. (1990). *Applied geophysics*. Cambridge university press.

Tikhonov, A. N. (1950, February). On determining electrical characteristics of the deep layers of the Earth's crust. In *Doklady* (Vol. 73, No. 2, pp. 295-297). Citeseer.

Uchida, T., & Sasaki, Y. (2006). Stable 3D inversion of MT data and its application to geothermal exploration. *Exploration Geophysics*, *37*(3), 223-230.

Vozoff, K. (1991). The magnetotelluric method. In *Electromagnetic methods in applied geophysics: Volume 2, application, parts A and B* (pp. 641-712). Society of exploration geophysicists.

Wamalwa, A. M., Mickus, K. L., & Serpa, L. F. (2013). Geophysical characterization of the Menengai volcano, Central Kenya Rift from the analysis of magnetotelluric and gravity data. *Geophysics*, *78*(4), B187-B199.

Wamalwa, A. M., & Serpa, L. F. (2013). The investigation of the geothermal potential at the Silali volcano, Northern Kenya Rift, using electromagnetic data. *Geothermics*, *47*, 89-96.

Wanjohi, A. W. (2014). Geophysical survey of a high-temperature field, Olkaria. *Short Course IX on Exploration for Geothermal Resources, organized by UNU-GTP, GDC and KenGen, Kenya*.

APPENDICES

Appendix I: Dimensionality analysis maps

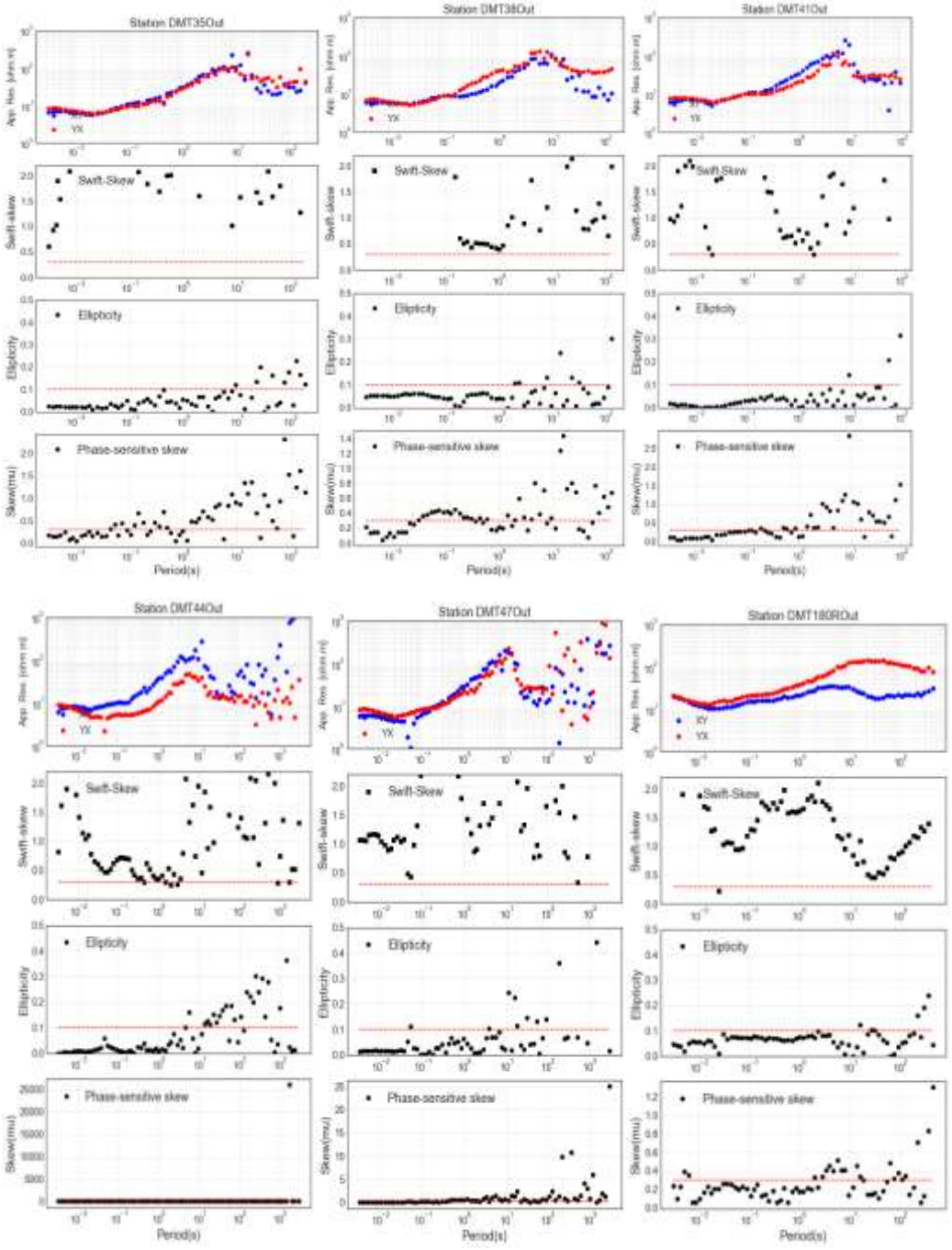

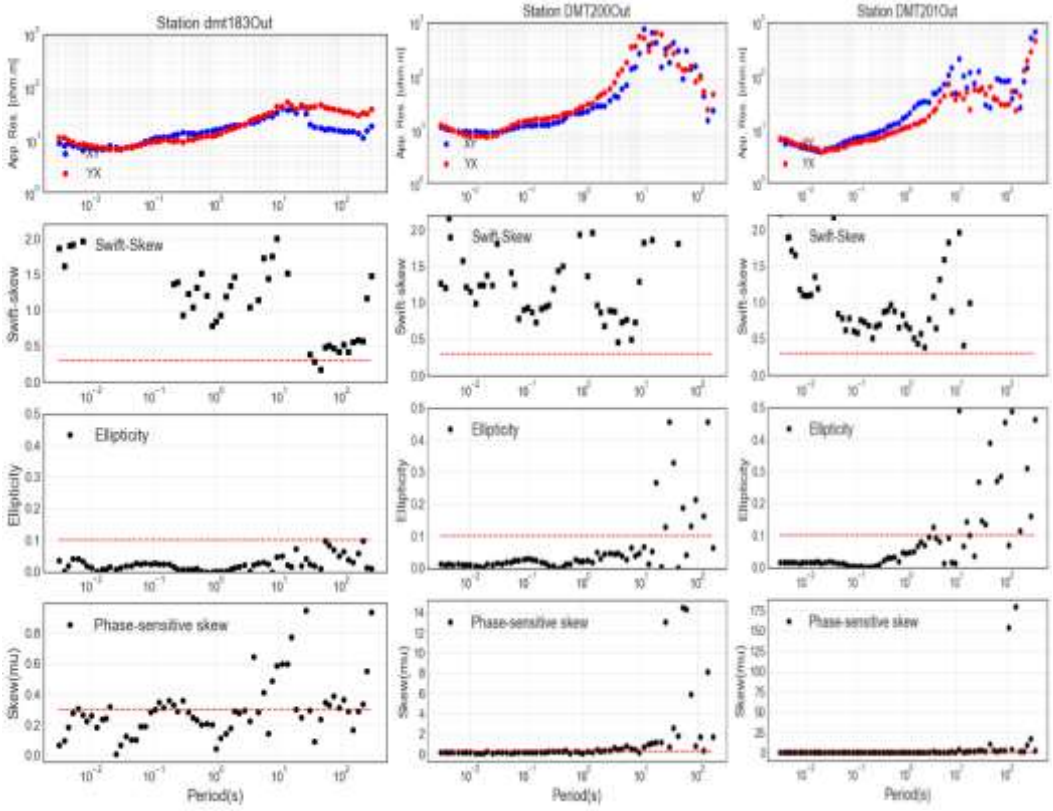
Station dmt183Out
Station DMT200Out
Station DMT201Out
App. Res. [ohm.m]
XY
YX
Swift-Skew
Swift-skew
Ellipticity
Phase-sensitive skew
Skew(mu)
Period(s)

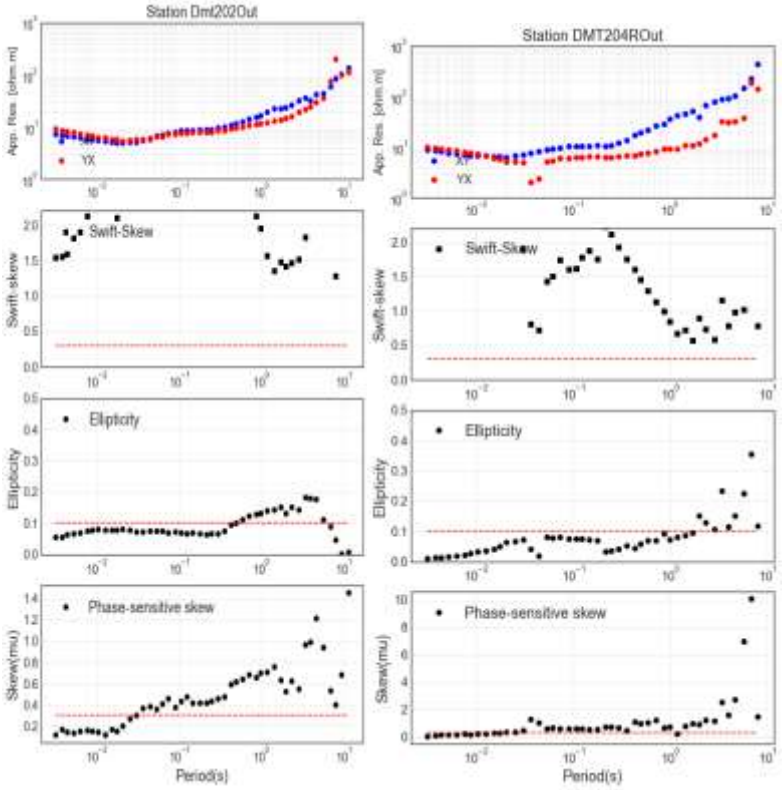
Station Dmt202Out
Station DMT204ROut
App. Res. [ohm.m]
XY
YX
Swift-Skew
Swift-skew
Ellipticity
Phase-sensitive skew
Skew(mu)
Period(s)

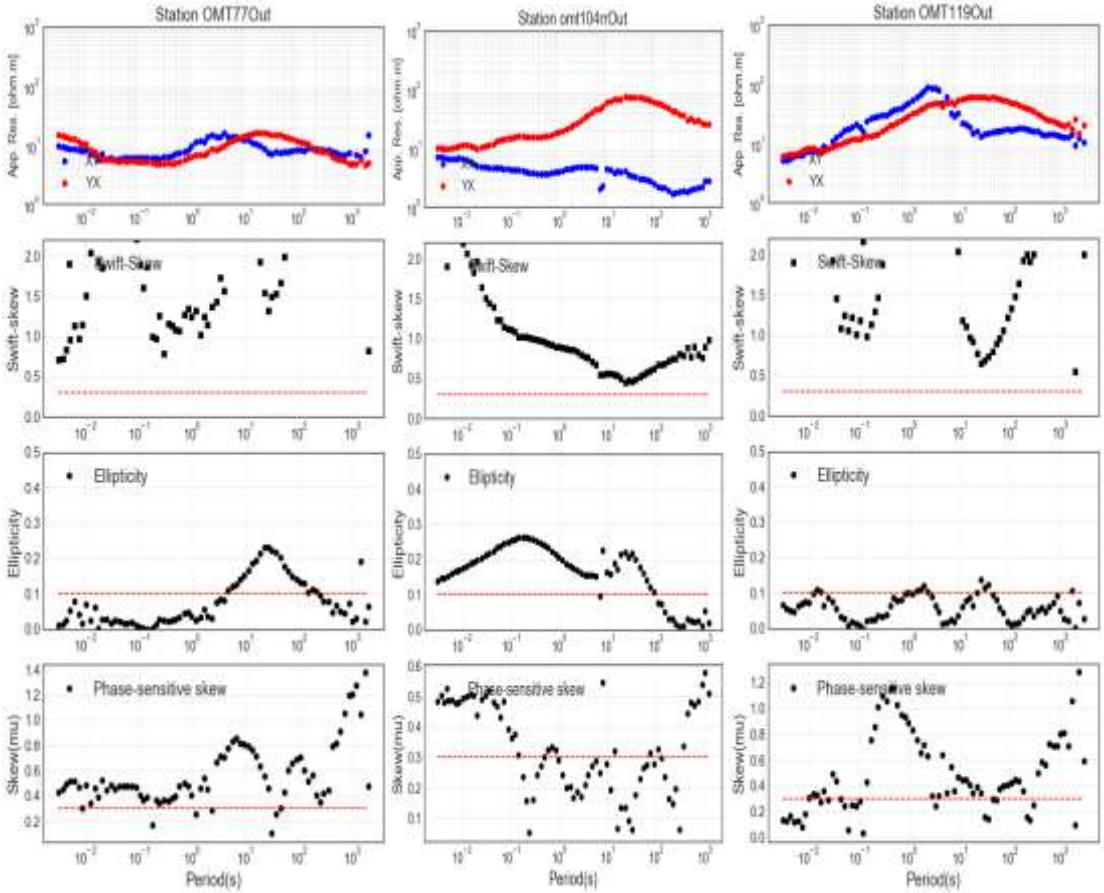
Station OMT77Out
Station omt104rOut
Station OMT119Out
App. Res. (ohm.m)
XY
YX
Swift-skew
Swift-Skew
Ellipticity
Phase-sensitive skew
Skew(rmu)
Period(s)

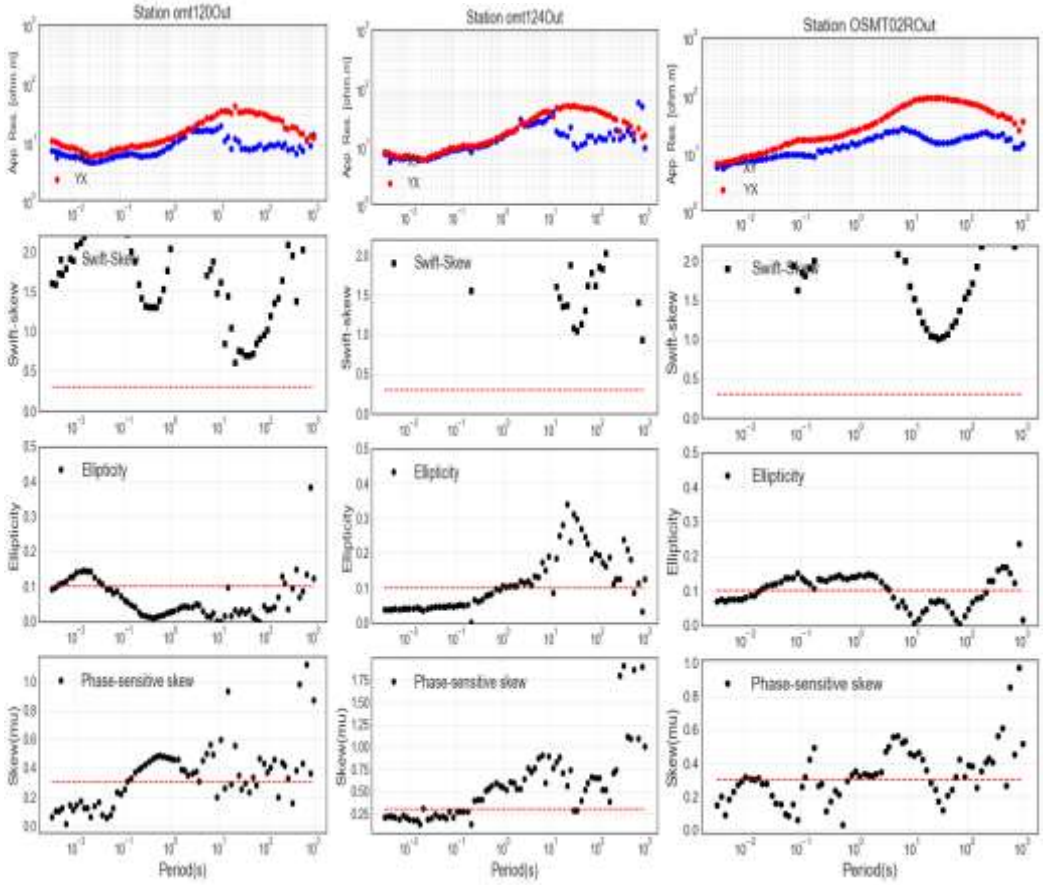
Station omt120Out
Station omt124Out
Station OSMT02ROut
App. Res. [ohm.m]
XY
YX
Swift-skew
Ellipticity
Phase-sensitive skew
Skew(mu)
Period(s)

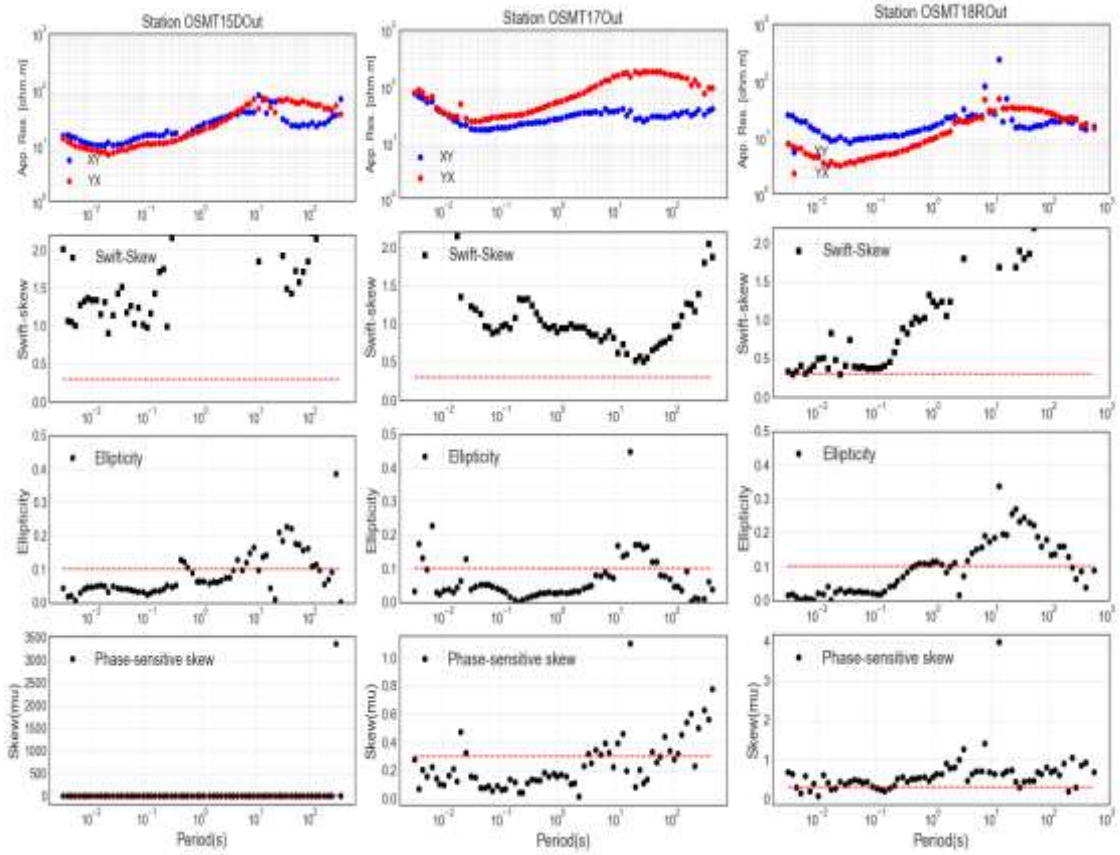
Station OSMT15DOut
Station OSMT17Out
Station OSMT18ROut
App. Res. [ohm.m]
XY
YX
Swift-Skew
Swift-skew
Ellipticity
Phase-sensitive skew
Skew(mu)
Period(s)

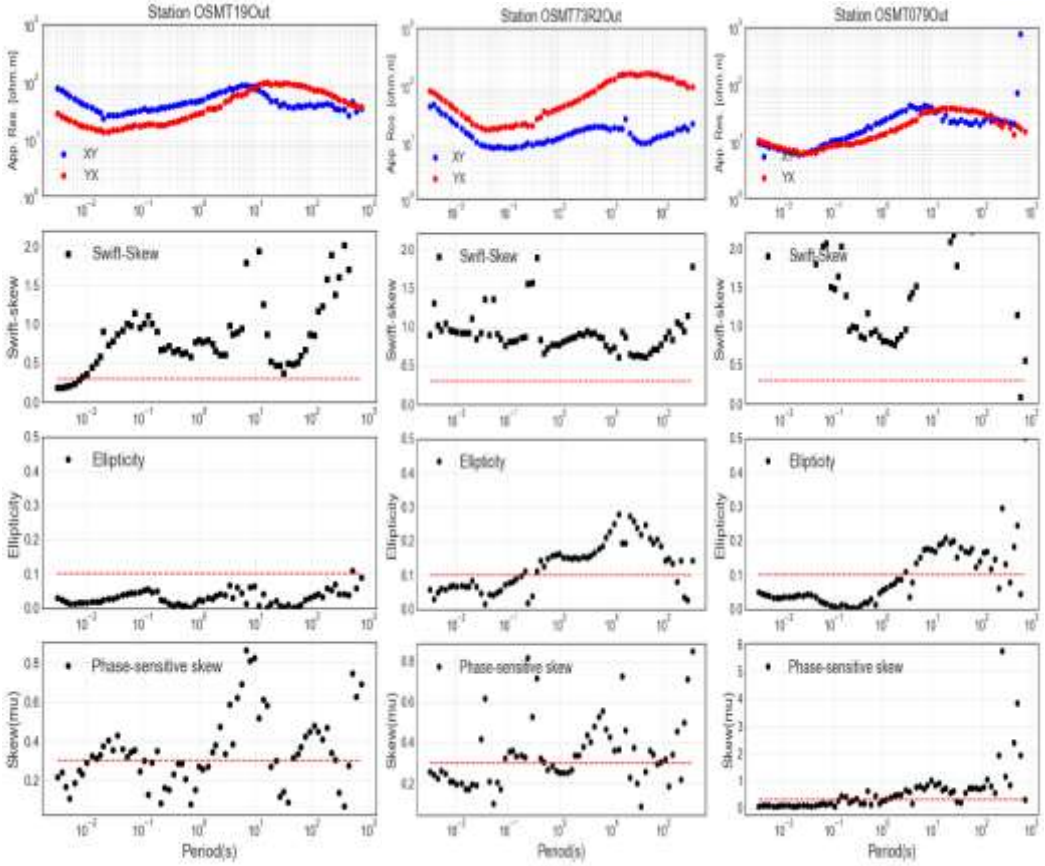
Station OSMT19Out
Station OSMT73R2Out
Station OSMT079Out
App. Res. [ohm.m]
XY
YX
Swift-Skew
Swift-skew
Ellipticity
Phase-sensitive skew
Skew(mu)
Period(s)

Appendix II: Static shift curves

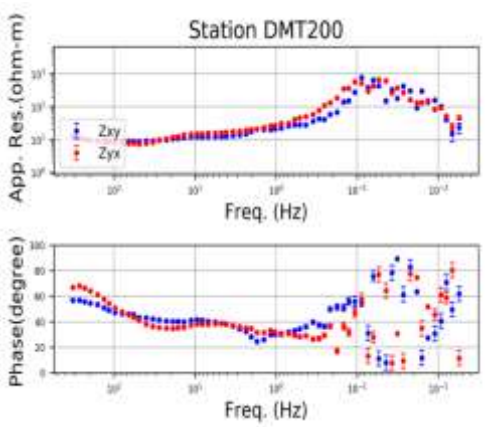

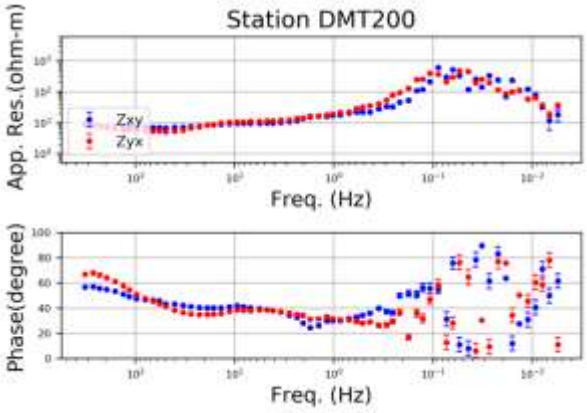

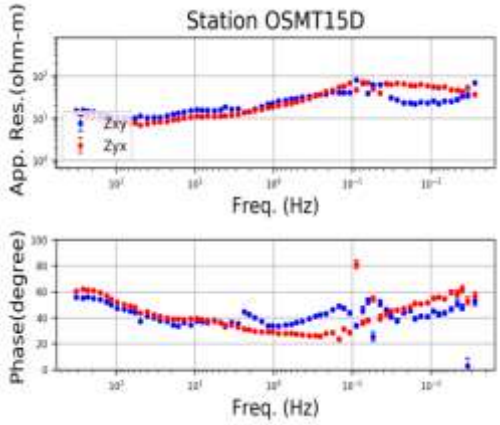

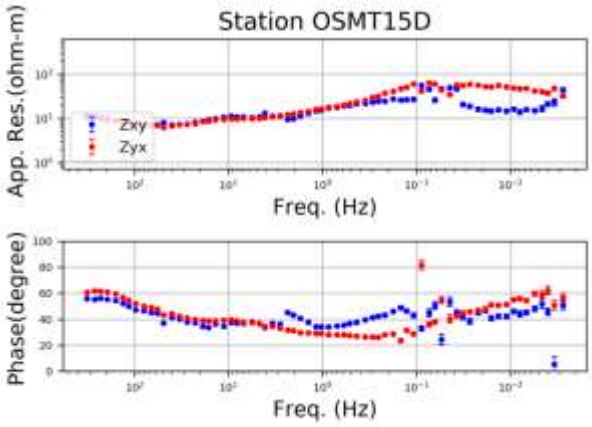

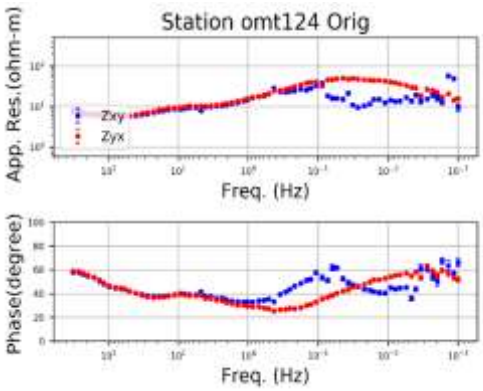
Station omt124 Orig
App. Res.(ohm-m)
Zxy
Zyx
Freq. (Hz)
Phase(degree)
Freq. (Hz)

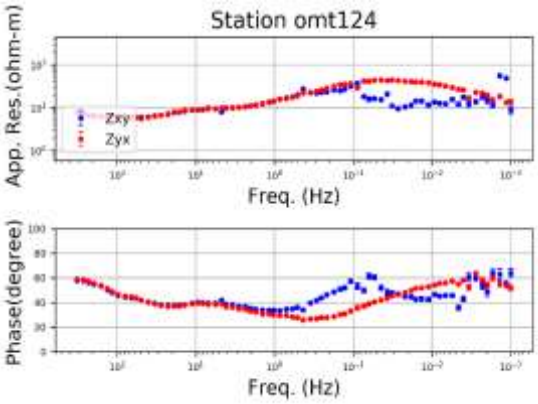
Station omt124
App. Res.(ohm-m)
Zxy
Zyx
Freq. (Hz)
Phase(degree)
Freq. (Hz)

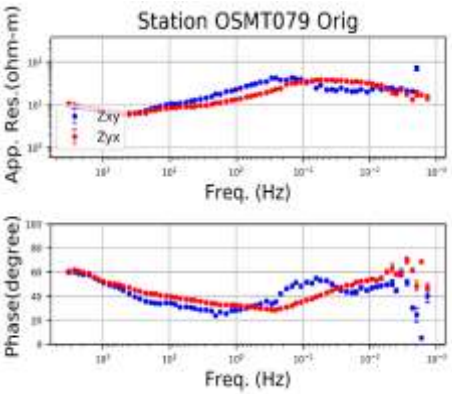
Station OSMT079 Orig
App. Res.(ohm-m)
Zxy
Zyx
Freq. (Hz)
Phase(degree)
Freq. (Hz)

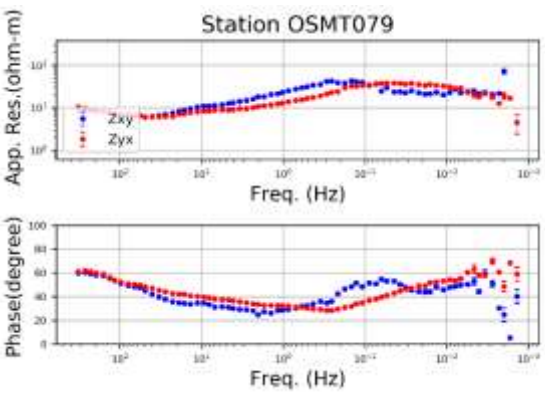
Station OSMT079
App. Res.(ohm-m)
Zxy
Zyx
Freq. (Hz)
Phase(degree)
Freq. (Hz)

Appendix III: 1D Curves

DMT 41

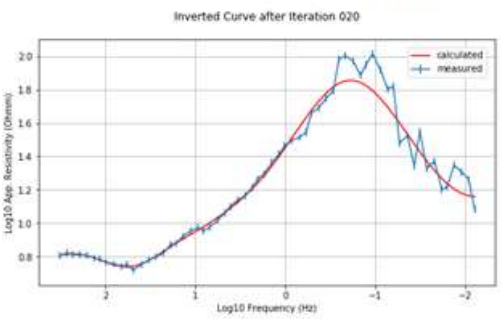

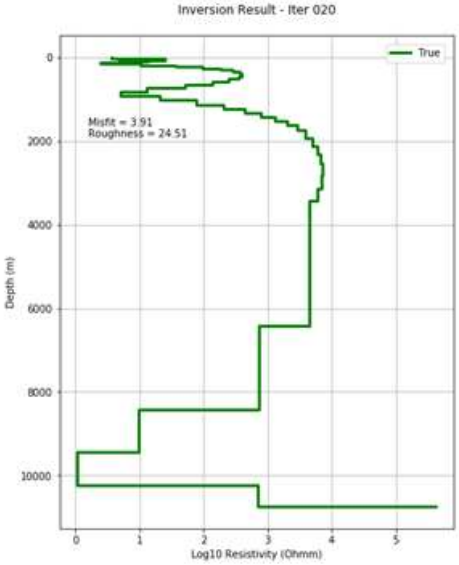

DMT 44

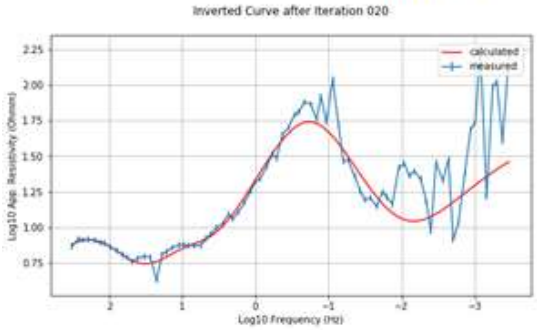

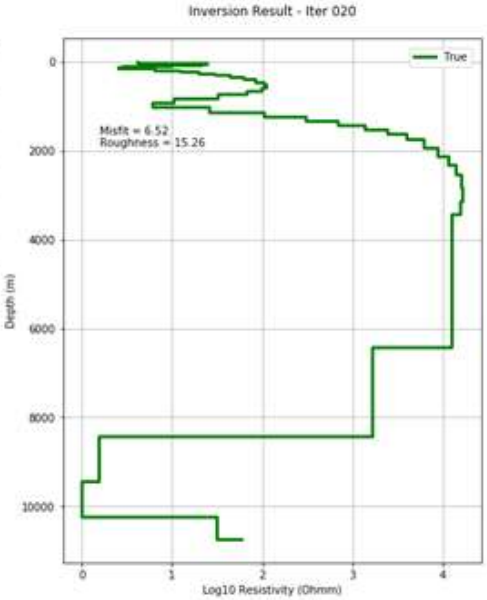

DMT 47

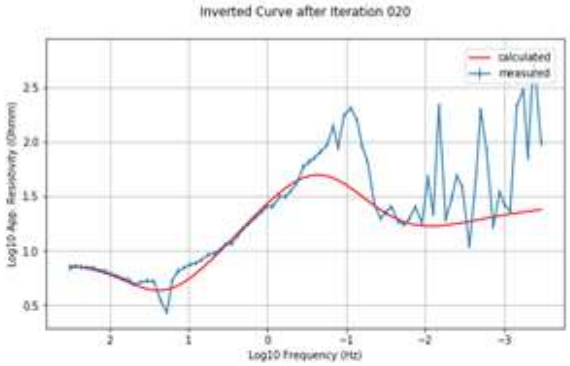

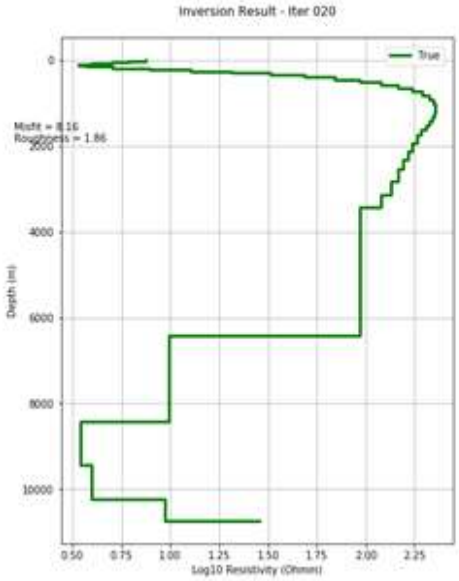

dmt 183

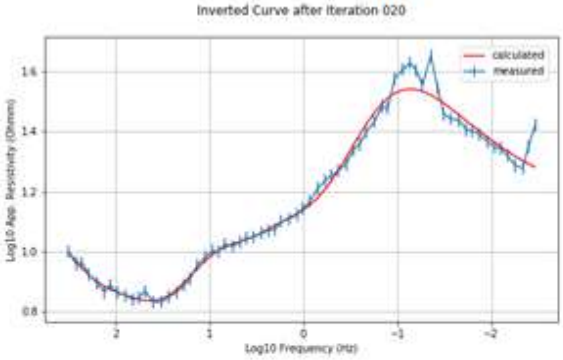

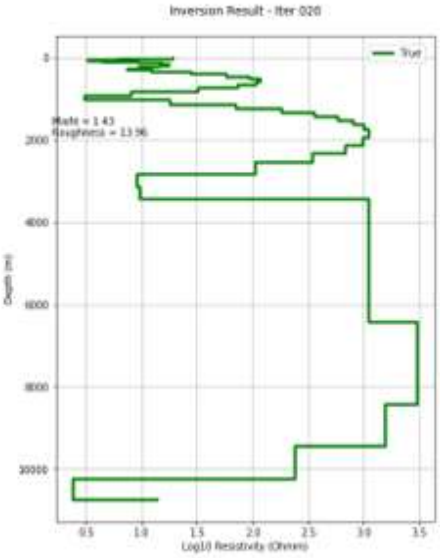

DMT 200

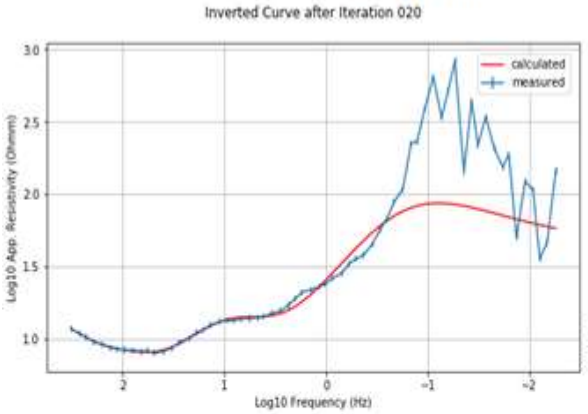

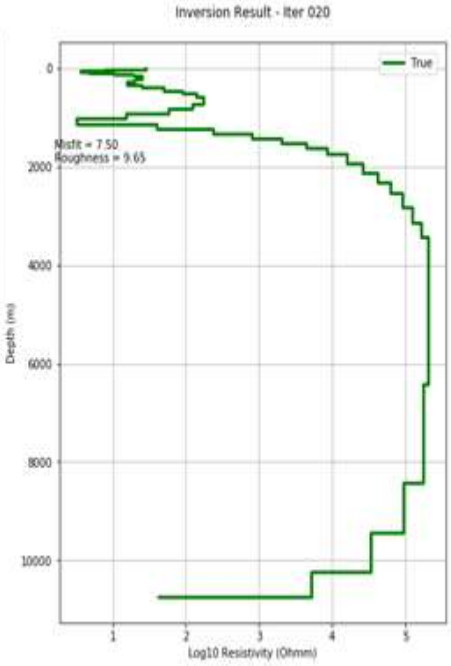

DMT 201

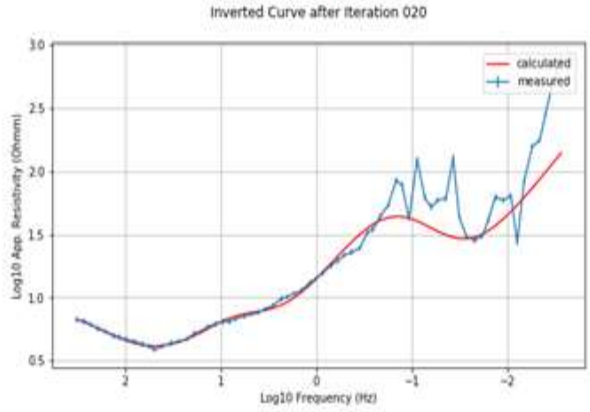

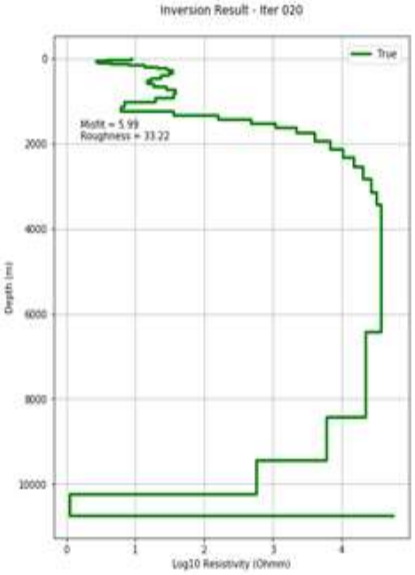

DMT 202

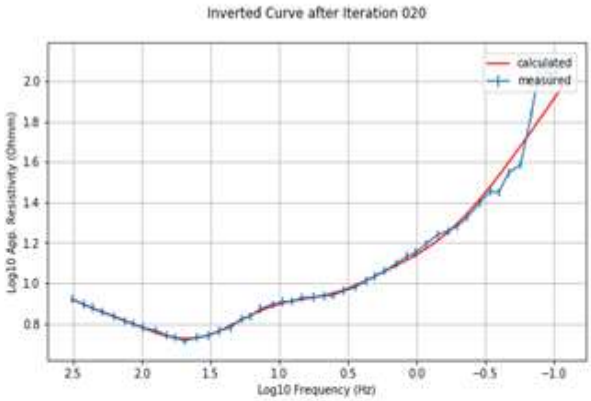

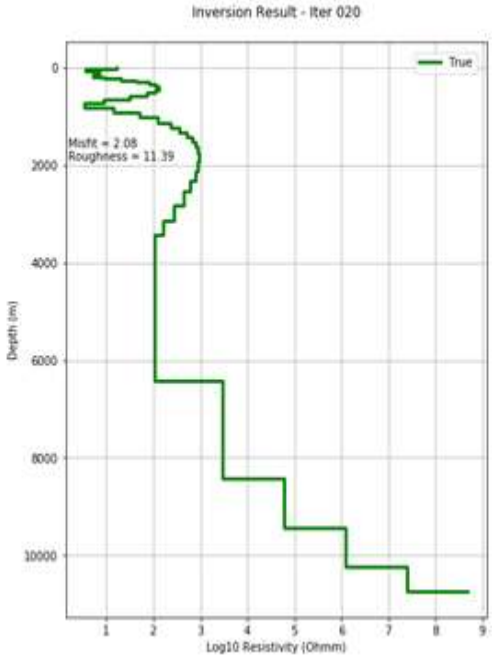

DMT 204

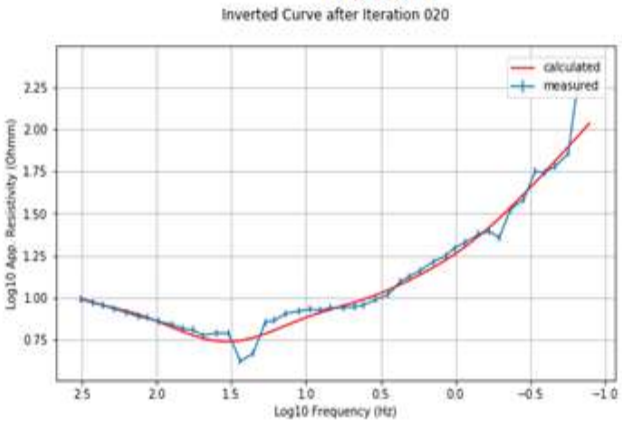

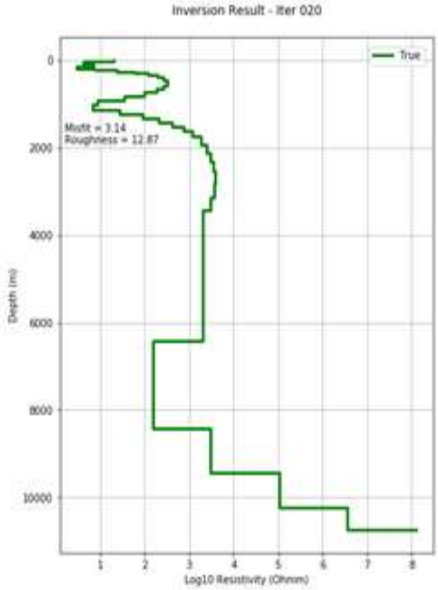

OMT 77

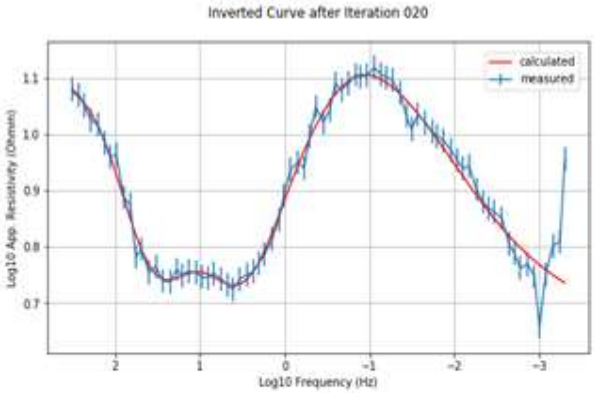

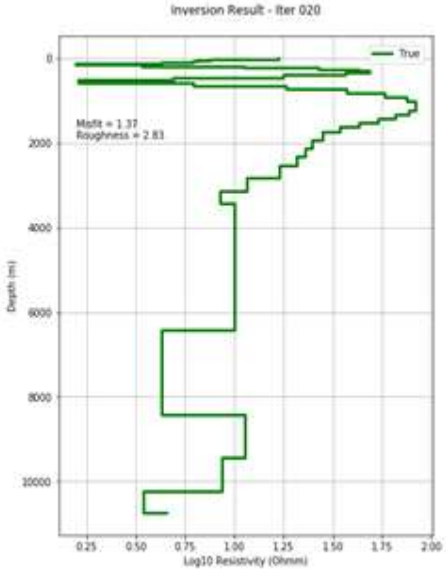

Omt 104rr

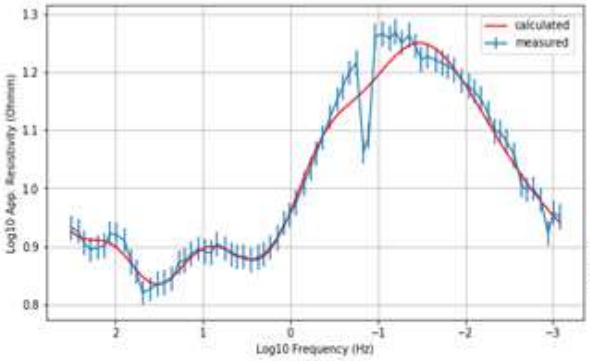

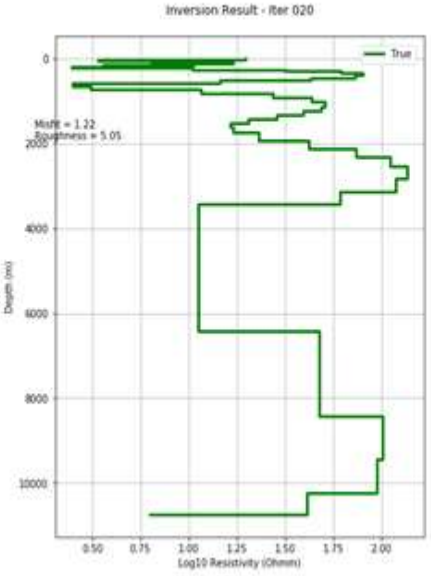

OMT 119

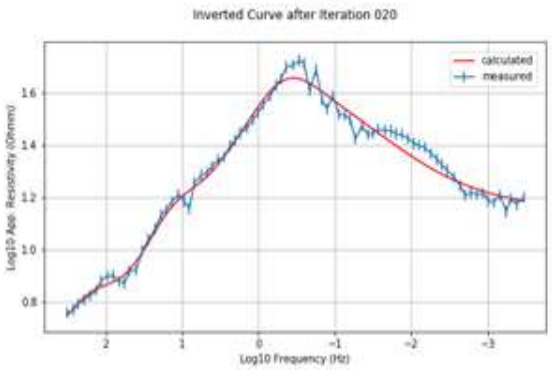

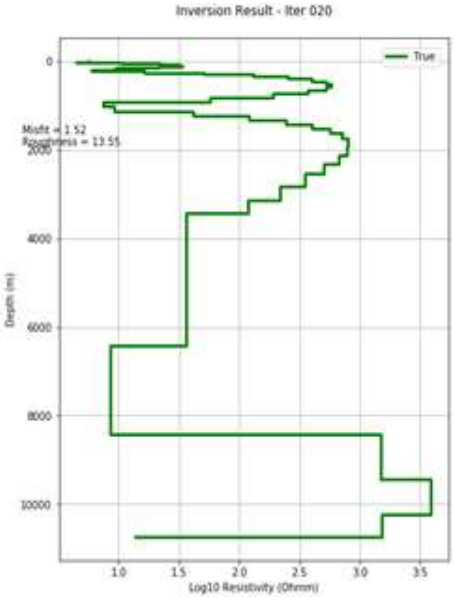

omt 124

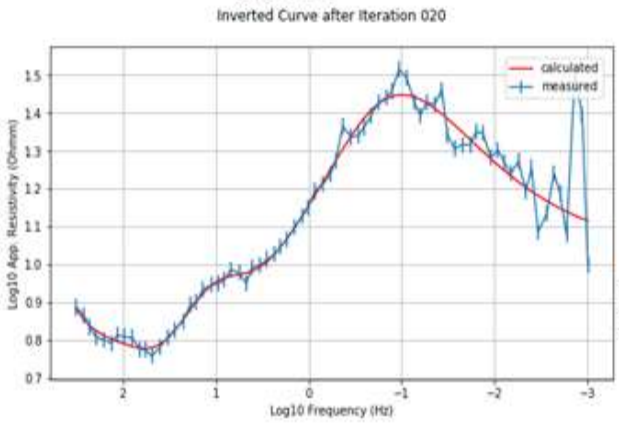

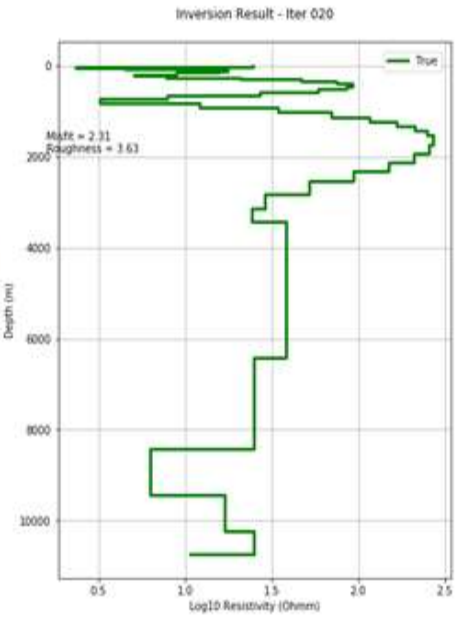

OSMT 02R

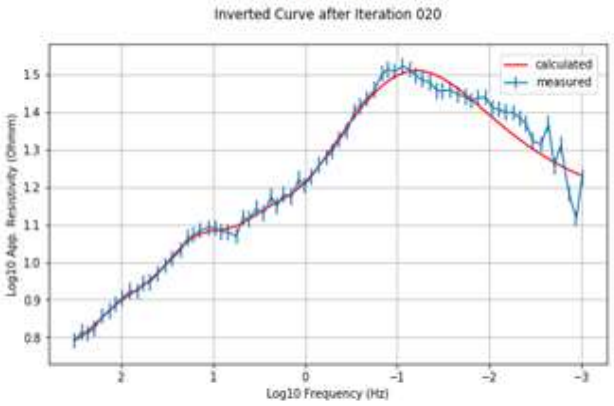

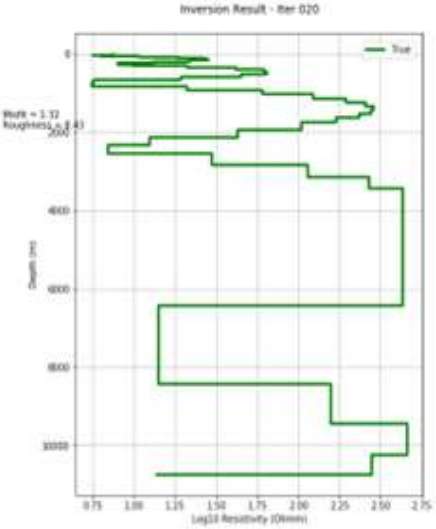

OSMT 15D